

First of all, we appreciate the reviewer's comments and suggestions. In response to the reviewer's comments, we have made relevant revisions to the manuscript. Listed below are our answers and the changes made to the manuscript according to the questions and suggestions given by the reviewer. Each comment of the reviewer (in black) is listed and followed by our responses (in blue).

Suggestions for revision or reasons for rejection (will be published if the paper is accepted for final publication)

The authors have addressed my previous comments. But based on the Authors' responses, I have the following further comments,

1. The domain size for domain 3 (inner most domain) is only 200kmX180 km, which is not a good configuration for MCS simulation. By definition, MCS at least covers more than 100 km raining region in one dimension with a fast-moving speed. So, to get the lifecycle of MCSs, you need a much larger domain than this.

In this study, we focus on heavy precipitation which mainly occurs during the mature stage of the simulated cloud system. The mature stage is between 20 LST and 23 LST on July 27th and the system at this mature stage is well captured by the domain as shown in Figure 8. Immediately after 4 LST on July 28th, which is after the mature stage and is a time included in the decaying stage, the system moves out of the domain and due to this, the whole decaying process is not captured by the domain. However, when time reaches a time point just before 4 LST on July 28th or immediately before the system moves out of the domain, there is near absence of heavy precipitation and thus we do not take interest in the period starting around 4 LST on July 28th. So, we believe that the domain adopted here is large enough to enable us to achieve our research goals mainly associated with the effects of aerosol on heavy precipitation.

In addition, MCS has its unique dynamics (it is different from thermal convection) and how much of the aerosols can be entrained into the system is always a concern. The analysis is also not connected with MCS dynamics such as the front-to-rear flow and rear inflow. Maybe the system was not a MCS? I think it is better not to call it a MCS to avoid confusion.

We just followed the definition of the MCS in Houze (1993). Houze (1993) defines an MCS as *"a cloud system that occurs in connection with an ensemble of thunderstorms and produces a contiguous precipitation area ~100 km or more in horizontal scale in at least one direction"*. We believe that the simulated cloud system satisfies this definition and thus can be considered an MCS, since this system is composed of thunderstorms that produce precipitation whose rates are as high as 180 mm hr⁻¹ at its mature stage and at its mature stage, the horizontal scale of precipitation area exceeds 100 km as shown in Figures 7 and 8.

It is true that we did not look at the ascending front-to-rear flow and the descending real inflow. However, we believe that our analyses themselves of downdrafts and outflow were enough to show how the strong convergence line and associated heavy precipitation form. We did not have to try to classify the inner dynamic structure into those flows and how each of those flows function, since even without this classification, we were able to identify a key mechanism that produces heavy precipitation and is associated with downdrafts, outflow, and aerosol effects on them through aerosol-induced changes in evaporation. Here, we want to say that aerosol is entrained into the system enough to cause the differences in evaporation and downdrafts between the western area and the eastern area in the domain, which in turn induce the strong convergence line and heavy precipitation, as shown in Figure 12.

According to Houze (1993), the ascending front-to-rear flow and the descending real inflow are characteristics of an MCS involving convective lines such as the squall lines. However, during the initial stage of cloud development between 17 and 19 LST (which leads to the development of the strong convergence), it is fair to say that there are no obvious convective lines but there are rather randomly spatially distributed cloud cells with high-level spatial inhomogeneity. Hence, it is likely that the mechanism which leads to the formation of the strong convergence is not associated with the systematic ascending front-to-rear flow and the descending real inflow that extend over the whole spatial scale of the system but with individual thermal convection in individual cells and localized circulation connecting those cells.

Reference:

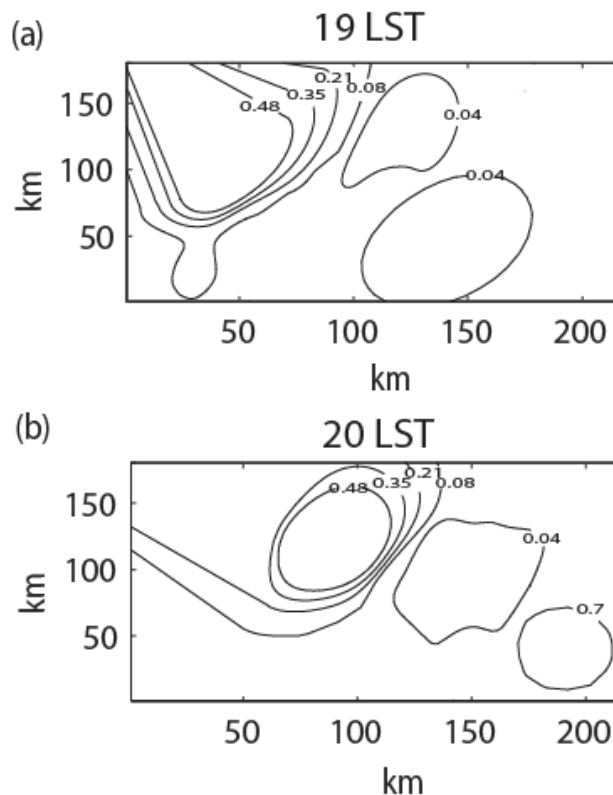
Houze, R. A., *Cloud dynamics*, Academic Press, 573 pp, 1993.

2. Based on what the authors clarified now, they did not really create an aerosol module. It is actually just an “aerosol preprocessor”. So it is more appropriate to call it “aerosol preprocessor”.

Aerosol module is replaced with aerosol preprocessor in text.

3. Even if the aerosol composition is not mainly black carbon or brown carbon, for polluted city like Seoul, AOD should be high and it would scatter a lot of solar radiation and cause surface cooling. I would suggest to add a plot for AOD. In the text, it is necessary to be clear that aerosol radiation interaction is not considered in this study and also discuss the uncertainty that this effect may cause such as the cooling at the surface would reduce the CAPE for convection.

As mentioned in text, we do not have high-resolution or 1-km resolution data for aerosol optical properties; we only have high-resolution data for PM10. Aerosol optical properties, which are needed for the calculation of AOD, are obtained only in AERONET sites which do not provide high-resolution data over the Seoul area. As mentioned in text, it is assumed that aerosol properties at the PM10 sites follow those measured by AERONET. With this assumption, AOD is obtained at the beginning stage of cloud system as shown in the following figure:



As seen in the figure above, there is higher AOD in the western part of the domain than in the eastern part. However, as described below and in text between line 841 and line 862 on pages 28-29, it is believed that the AOD distribution does not play an important role in results here.

The following is added to clarify the fact that aerosol-radiation interactions are not considered:

(LL250-255 on p9)

In this study, aerosol-radiation interactions, which are the effect of aerosol on radiation via the reflection, scattering and absorption of shortwave and longwave radiation by aerosol

before its activation, are not considered. This is partially motivated by the fact that the mixture includes chemical components that absorb solar radiation insignificantly as compared to strong radiation absorbers such as black carbon.

The following is added to discuss the uncertainty associated with no consideration of aerosol-radiation interactions:

(LL841-862 on p28-29)

As mentioned, observed aerosol particles include components which do not absorb radiation significantly, hence, the aerosol absorption of radiation is not considered in this study. However, ammonium sulfate and organic compound, which are observed to comprise aerosol here, reflect and scatter radiation, although these reflection and scattering are not considered in this study. The reflection and scattering of particularly solar radiation by aerosol decrease solar radiation that reaches the surface and thus surface fluxes. Higher aerosol concentrations in the western part of the domain can cause more reflection and scattering of solar radiation by aerosol than in the eastern part. This can reduce surface fluxes, the associated convection intensity, condensation, and transportation of cloud liquid to unsaturated areas by convective motion in the western part more than in the eastern part. As a result, there can be reduction in the contrast in evaporative cooling between the parts as compared to the contrast with no consideration of the reflection and scattering. This can lower the intensity and frequency of heavy precipitation by diminishing the contrast in wind field between the parts. However, the simulated intensity and frequency of heavy precipitation with no consideration of the reflection and scattering by aerosol are not that deviant from observed counterparts. This indicates that the effect of the reflection and scattering by aerosol, and associated changes in surface fluxes on heavy precipitation is likely to be insignificant in reality. This is likely to be due to the fact that once deep clouds with high-value cloud fraction and cloud optical depth form, the effect of aerosol on radiation is taken over by that of clouds on radiation, which leads to a situation where aerosol effects on radiation become negligible as compared to cloud effects on radiation.

4. The 1 micro aerosol particle is already in coarse mode. Accumulation mode peaks usually at 100-200 nm. It is even important to get the Aitken mode right for strong convection. With PM10, uncertainties in both accumulation and Aitken modes would be very large. Based on the SD plot in Figure 3, smaller particles (Aitken model) aerosols are dominant in number concentrations.

Did those small particles get activated?

Yes, a small portion of Aitken-mode aerosol particles or small particles with diameter smaller than 0.1 micron are activated when there is unusual high-level supersaturation.

What is the total aerosol number (should be provided for each case) at low-level and what size of the aerosols can be activated? A recent study (Fan et al. 2018, Science) showed that very small particles from urban plume can be activated and enhance condensation heating significantly. This would enhance the convective intensity and precipitation rates at the convective region, both of which can lead to strong downdrafts as well. So the stronger downdrafts might not just be due to the larger evaporative cooling as the authors claimed. I would suggest looking at this aspect by looking at the changes in nucleation and condensation heating.

The total aerosol number concentration around the surface is shown in Figure 4. As shown in Figures 4 and 8, the western part of the domain is already polluted by aerosol in the background at the initial stage of cloud development, which is contrary to the situation in Fan et al. (2018) where the background is in clean condition at the initial stage. Hence, there is already delayed autoconversion at the very beginning of cloud development in the case here, which is again contrary to the situation in Fan et al. (2018). This induces high-value cloud droplet number concentration (CDNC) and thus increases competition for water vapor among droplets, preventing the occurrence of high-value supersaturation and thus preventing the activation of a large portion of small, particularly, Aitken-mode aerosol particles. Hence, in this study, the contribution of Aitken-mode aerosol particles to the droplet nucleation is insignificant, which is different from Fan et al. (2018). Also, we want to say that this study just focuses on the effects of inhomogeneity of the spatial distribution of aerosol loading itself or the total aerosol concentration itself on clouds and precipitation and whether Aitken-mode aerosol plays an important role in those effects is out of scope of this study. However, it is true that due to higher-value CDNC in the western part of the domain, there is the greater total surface area of droplets, inducing greater condensation (occurring on the surface of droplets), as compared to those in the eastern part of the domain. This point is indicated as follows:

(LL543-552 on p18-19)

In addition, high-value aerosol concentrations produce high-value cloud droplet number concentration and the associated high-value surface areas of droplets. The surface of droplets is where condensation occurs and as shown by Lee et al. (2009) and a recent study by Fan et al. (2018), the high-value surface areas cause higher-value condensation as compared to the situation with low-value aerosol concentrations that lead to lower-value condensation. The averaged condensation rate over the above-mentioned area to the west (east) of the strong convergence field and over the period between 17:00 and 19:00 LST is

1.28 (0.97) $\text{g m}^{-3} \text{h}^{-1}$ in the control run. This further increases cloud liquid (as a source of evaporation) and thus its evaporation in the area with high-value aerosol concentrations.

Finally, we want to say that rain evaporation, associated with precipitation rate, is not a factor which causes the strong downdrafts and convergence; for details, see Figure 12a and related text.

5. What do you mean by “we zero in on condensation” in Line 499?

It means among sources of precipitation, which are condensation, deposition, and freezing, we mainly focus on condensation. The text is revised to clarify this point.

1 **Aerosol as a potential factor to control the increasing torrential rain events in urban**
2 **areas over the last decades**

3 Deleted: ¶

4 Deleted: ¶

5 Seoung Soo Lee¹, Byung-Gon Kim², Zhanqing Li¹, Yong-Sang Choi³, Chang-Hoon

6 Jung⁴, Junshik Um⁵, Jungbin Mok¹, Kyong-Hwan Seo⁵

7

8 ¹Earth System Science Interdisciplinary Center, University of Maryland, Maryland

9 ²Department of Atmospheric Environmental Sciences, Gangneung-Wonju National

10 University, Gangneung, Gang-Won do, South Korea

11 ³Department of Environmental Science and Engineering, Ewha Womans University,

12 Seoul, South Korea

13 ⁴Department of Health Management, Kyungin Women's University, Incheon, South

14 Korea

15 ⁵Department of Atmospheric Sciences, Division of Earth Environmental System,

16 Pusan National University, Busan, Korea

17

18

19 Deleted: ¶

20 Corresponding author: Seoung Soo Lee

21 Office: (303) 497-6615

22 Cell: (609) 375-6685

23 Fax: (303) 497-5318

24 E-mail: cumulss@gmail.com, slee1247@umd.edu

25

39 **Abstract**

40

41 This study examines the role played by aerosol in torrential rain that occurred in the
42 Seoul area, which is a conurbation area where urbanization has been rapid in the last few
43 decades, using cloud-system resolving model (CSRМ) simulations. The model results
44 show that the spatial variability of aerosol concentrations causes the inhomogeneity of the
45 spatial distribution of evaporative cooling and the intensity of associated outflow around
46 the surface. This inhomogeneity generates a strong convergence field in which torrential
47 rain forms. With the increases in the variability of aerosol concentrations, the occurrence
48 of torrential rain increases. This study finds that the effects of the increases in the
49 variability play a much more important role in the increases in torrential rain than the
50 much-studied effects of the increases in aerosol loading. Results in this study demonstrate
51 that for a better understanding of extreme weather events such as torrential rain in urban
52 areas, not only changing aerosol loading but also changing aerosol spatial distribution
53 since industrialization should be considered in aerosol-precipitation interactions.

54

55

56

57

58

59

60

61

62

63

64

65

66

67

68

69

1. Introduction

70
71
72 It has been reported that there has been an increase in the frequency of torrential rain in
73 urban areas over the last decades (Bouvette et al., 1982; Diem and Brown, 2003; Fujibe,
74 2003; Takahashi, 2003; Burian and Shepherd, 2005; Shepherd, 2005; Chen et al., 2015).
75 Over the last decades, population in urban areas has increased significantly. In 1950, 30 %
76 of the whole population in the world lived in urban areas, however, in 2010, 54 % of the
77 whole population lived in urban areas. It is predicted that in 2050, 66 % of the whole
78 population will live in urban areas (United Nations, 2015). In addition, urban areas are
79 the centers of economic activity and play a key role in economic productivity (United
80 Nations, 2015). Hence, the increase in the frequency of torrential rain, which has
81 substantial negative impacts on human life and properties by causing events such as
82 flooding and landslide, particularly in urban areas has important social and economic
83 implications.

84 Torrential rain in urban areas frequently involves highly inhomogeneous spatial
85 distributions of precipitation (Dhar and Nandergi, 1993; Mannan et al., 2013). While
86 some places in a metropolitan area experience light precipitation, others in the area
87 experience extremely heavy precipitation or torrential rain for an identical mesoscale
88 convective system (MCS) that covers the whole area (e.g., Sauer et al., 1984; Korea
89 Meteorological Administration, 2011). Note that this type of the MCS is forced by
90 synoptic-scale temperature and humidity forcings. These “synoptic-scale” forcings tend
91 to be spatially homogeneous in the MCS whose spatial scale is at mesoscale and thus
92 much smaller than that of the forcings. Hence, these forcings tend to intensify all of cloud
93 cells in the MCS in an approximately homogeneous fashion, which tend to produce cloud
94 cells with a similar intensity. These cloud cells with the similar intensity are likely to
95 result in a homogeneous distribution of precipitation over a domain of interest, since
96 cloud cells with the similar intensity are likely to produce similar precipitation. This
97 indicates that the consideration of the synoptic-scale forcings alone is not able to explain
98 the occurrence of torrential rain which is associated with inhomogeneous spatial
99 distributions of precipitation. Note that numerous numerical weather prediction studies
100 have utilized the concept of the synoptic-scale forcings to identify mechanisms that

101 control the inhomogeneity of precipitation distributions and associated torrential rain.
102 This is one of the reasons these studies have shown low forecast accuracy for torrential
103 rain and not been able to provide a clear picture of the mechanisms (Mladek et al., 2000;
104 Yeh and Chen, 2004; Mannan et al., 2013). The highly inhomogeneous distribution of
105 precipitation means that there are highly inhomogeneous variables, processes and
106 forcings which disrupt the synoptic-forcing-induced homogeneity of MCSs in urban areas.
107 Some of those forcings are mesoscale forcings that show mesoscale variability and, for
108 example, are related to phenomena such as sea-breeze fronts and lake breezes. In
109 particular, in urban areas, due to strong heat fluxes at the surface, there is the urban heat
110 island (UHI) effect as another example of those phenomena. Examples of those variables
111 and processes are cold pool, rear inflow, wind shear, and mesoscale vorticity. Aerosol is
112 also one of those variables which have large spatial variability. In particular, urban
113 aerosol particles are produced by randomly distributed sources (e.g., traffic), which
114 enables aerosol to have large variability in urban areas.

115 It is well-known that increasing aerosol loading alters cloud microphysical
116 properties such as cloud-particle size and autoconversion. Cloud-liquid particles, which
117 are droplets, collide and collect each other to grow to be raindrops and this growth
118 process is referred to as autoconversion. Collision and collection are more efficient when
119 particle sizes are larger. Hence, increasing aerosol loading, which is known to reduce the
120 particle size, reduces the efficiency of the growth of cloud-liquid particles to raindrops
121 via autoconversion. This results in more cloud liquid which is not grown to be converted
122 to raindrops and thus in more cloud-liquid mass as a source of evaporation and freezing.
123 It has been shown that aerosol-induced increases in cloud-liquid mass and associated
124 increases in freezing of cloud liquid can enhance parcel buoyancy and thus invigorate
125 convection (Khain et al., 2005; Rosenfeld et al., 2008; Li et al., 2011; Wang et al., 2014).
126 Invigorated convection can enhance precipitation. Studies (e.g., van den Heever et al.,
127 2006; Fan et al., 2009; Lebo and Seinfeld, 2011; Lebo, 2017) have shown that aerosol-
128 induced invigoration of convection and enhancement of precipitation depend on
129 competition between aerosol-induced increases in buoyancy and those in hydrometeor
130 loading, and aerosol-induced increases in condensational heating and associated
131 invigoration in the warm sector of a cloud system. Other studies (e.g., Khain et al., 2008;

132 Lee et al., 2008b; Fan et al., 2009) have shown that the invigoration-related enhancement
133 of precipitation also depends on environmental conditions that are represented by wind
134 shear, relative humidity, and instability.

135 Aerosol-induced increases in cloud-liquid mass and associated increases in
136 evaporation can intensify gust fronts, which in turn intensify subsequently developing
137 convective clouds and enhance precipitation (Khain et al., 2005; Seifert and Beheng,
138 2006; Tao et al., 2007; van den Heever and Cotton, 2007; Storer et al., 2010; Tao et al.,
139 2012; Lee and Feingold, 2013; Lee et al., 2017). Aerosol-induced invigoration and
140 intensification of convection and associated convective clouds raise a hypothesis that the
141 large spatial variability of aerosol in tandem with increasing aerosol loading can generate
142 and enhance torrential rain which can involve the inhomogeneity of precipitation and
143 associated cloud intensity in urban areas. For example, cloud cells (in an MCS) sitting on
144 a significant portion of a metropolitan area with a higher aerosol concentration can be
145 invigorated more than those cells on the rest portion of the area with a lower aerosol
146 concentration. This can lead to enhanced precipitation and possibly torrential rain at the
147 portion with the higher aerosol concentration, while in the rest portion, there can be less
148 precipitation. This creates an inhomogeneity of precipitation distributions that can
149 accompany torrential rain in the specific portion of the area. A further increase in aerosol
150 concentration in the portion with the higher aerosol concentration will further enhance
151 precipitation and torrential rain there and thus create a greater inhomogeneity of
152 precipitation distributions. Motivated by the hypothesis and associated argument here,
153 among the forcings, processes and variables which have spatial variability, this study
154 focuses on aerosol. To examine aerosol effects on clouds and precipitation, numerical
155 simulations are performed by using a cloud-system resolving model (CSRМ) that
156 resolves cloud-scale microphysical and dynamic processes and simulates the effect of the
157 variability and loading of aerosol on precipitation.

158 Using the CSRМ, an observed MCS that involves deep convective clouds and
159 torrential rain is simulated. Here, deep convective clouds reach the tropopause. For the
160 simulations, we select an MCS over the Seoul area (in Korea) that has a population of ~
161 twenty five millions and thus is one of representative conurbation areas around the world.
162 These simulations are to identify key mechanisms that are associated with cloud-scale

163 microphysics and dynamics and explain the generation of the inhomogeneity of
164 precipitation and associated torrential rain in terms of the spatial variability and loading
165 of aerosol.

166

167 **2. Case description**

168

169 The MCS was observed in the Seoul area, Korea over a period between 09:00 LST (local
170 solar time) July 27th and 09:00 LST July 28th 2011. A significant amount of
171 precipitation is recorded during this period, with a local maximum value of ~ 200.0 mm
172 hr^{-1} . This heavy rainfall caused flash floods and landslides, leading to the deaths of 60
173 people (Korea Meteorological Administration, 2011). At 21:00 LST July 26th 2011,
174 favorable synoptic-scale features for the development of the selected MCS and heavy
175 rainfall were observed. The western Pacific subtropical high (WPSH) was located over
176 the southeast of Korea and Japan, and there was a low-pressure trough over north China
177 (Figure 1). Low-level jets between the flank of the WPSH and the low-pressure system
178 brought warm, moist air from the Yellow Sea to the Korean Peninsula (Figure 1).
179 Transport of warm and moist air by the southwesterly low-level jet is an important
180 condition for the development of heavy rainfall events over the Korean Peninsula
181 (Hwang and Lee 1993; Lee et al. 1998; [Seo et al. 2013](#)).

182

183

184 **3. CSRM and simulations**

185

186 **3.1 CSRM**

187

188 As a CSRM, we use the Advanced Research Weather Research and Forecasting (ARW)
189 model (version 3.3.1), which is a nonhydrostatic compressible model. Prognostic
190 microphysical variables are transported with a 5th-order monotonic advection scheme
191 (Wang et al., 2009). Shortwave and longwave radiation parameterizations have been
192 included in all simulations by adopting the Rapid Radiation Transfer Model (RRTMG;
193 Mlawer et al., 1997; Fouquart and Bonnel, 1980). The effective sizes of hydrometeors are

Deleted: un and Lee 2002

195 calculated in a microphysics scheme that is adopted by this study and the calculated sizes
196 are transferred to the RRTMG. Then, the effects of the effective sizes of hydrometeors on
197 radiation are calculated in the RRTMG.

198 To represent microphysical processes, the CSRМ ~~employs~~ a bin scheme. The bin
199 scheme ~~employed~~ is based on the Hebrew University Cloud Model (HUCM) described
200 by Khain et al. (2011). The bin scheme solves a system of kinetic equations for size
201 distribution functions for water drops, ice crystals (plate, columnar and branch types),
202 snow aggregates, graupel and hail, as well as cloud condensation nuclei (CCN). Each size
203 distribution is represented by 33 mass doubling bins, i.e., the mass of a particle m_k in the
204 k bin is determined as $m_k = 2m_{k-1}$.

Deleted: adopts

Deleted: adopted

205

206 3.2 Control run

207

208 For a three-dimensional simulation of the observed MCS, i.e., the control run, two-way
209 interactive triple-nested domains with a Lambert conformal map projection as shown in
210 Figure 2 is adopted. A domain with a 500-m resolution covering the Seoul area (Domain
211 3) is nested in a domain with a 1.5-km resolution (Domain 2), which in turn is nested in a
212 domain with a 4.5-km resolution (Domain 1). The length of Domain 3 in the east-west
213 direction is 220 km, while the length in the north-south direction is 180 km. The lengths
214 of Domain 2 and Domain 3 in the east-west direction are 390 and 990 km, respectively,
215 and those in the north-south direction are 350 and 1100 km, respectively. The Seoul area
216 is a conurbation area that centers in Seoul and includes Seoul and surrounding highly
217 populated cities. Hence, the Seoul area is composed of multiple cities whose total
218 population is ~twenty five millions. The boundary of Seoul, which has the largest
219 population among those cities, is marked by a dotted line in Figure 2. Black contours in
220 Figure 2 represent terrain heights. They indicate that most of high terrain is located on the
221 eastern part of the Korean Peninsula and the Seoul area is not affected by high terrain. All
222 domains have 84 vertical layers with a terrain following sigma coordinate, and the model
223 top is 50 hPa. Note that a cumulus parameterization scheme is used in Domain 1 but not
224 used in Domain 2 and Domain 3 where convective rainfall generation is assumed to be
225 explicitly resolved. Here, we use a cumulus parameterization scheme that was developed

228 by Kain and Fritsch (1990 and 1993). This scheme is shown to work reasonably well for
229 resolutions that are similar to what is used for Domain 1 (Gilliland and Rowe, 2007).

230 Reanalysis data, which are produced by the Met Office Unified Model (Brown et
231 al., 2012) and recorded continuously every 6 hours on a $0.11^\circ \times 0.11^\circ$ grid, provide the
232 initial and boundary conditions of potential temperature, specific humidity, and wind for
233 the simulation. These data represent the synoptic-scale environment. For the control run,
234 we employ an open lateral boundary condition. Using the Noah land surface model (LSM;
235 Chen and Dudhia, 2001), surface heat fluxes are predicted.

Deleted: adopt

236 The current version of the ARW model assumes horizontally homogeneous aerosol
237 properties. For the control run that focuses on the effect of aerosol on torrential rain in an
238 urban area (i.e., Seoul area) where aerosol properties such as composition and number
239 concentration vary significantly in terms of time and space, we abandon this assumption
240 of homogeneity and consider the spatiotemporal variability of aerosol properties over the
241 urban area. For this, we develop an aerosol preprocessor, that is able to represent the
242 variability of aerosol properties. This aerosol preprocessor, interpolates observed
243 background aerosol properties such as aerosol mass (e.g., PM_{10}) at observation sites to
244 model grid points and time steps. This aerosol preprocessor is now implemented to the
245 ARW model.

Deleted: module

Deleted: module

Deleted: module

246 The variability of aerosol properties is observed by surface sites that measure PM_{10}
247 in the Seoul area. These sites are distributed with about 1 km distance between them and
248 measure aerosol mass every ~10 minutes, which enables us to resolve the variability with
249 high spatiotemporal resolutions. However, the measurement of other aerosol properties
250 such as aerosol composition and size distributions at those sites is absent. There are
251 additional sites of the aerosol robotic network (AERONET; Holben et al., 2001) in the
252 Seoul area. Distances between these AERONET sites are ~10 km, hence, they do not
253 provide data whose resolutions are as high as those of the PM_{10} data. However, the
254 AERONET sites provide information on aerosol composition and size distributions.
255 While using data from the high-resolution PM_{10} sites to represent the variability of
256 aerosol properties over the Seoul area, we use the relatively low-resolution data from the
257 AERONET sites to represent aerosol composition and size distributions.

262 AERONET measurements indicate that overall, aerosol particles in the Seoul area
 263 during the MCS period follow a tri-modal log-normal distribution and aerosol particles,
 264 on average, are an internal mixture of 60 % ammonium sulfate and 40 % organic
 265 compound. This organic compound is assumed to be water soluble and composed of (by
 266 mass) 18 % levoglucosan ($C_6H_{10}O_5$, density = 1600 kg m^{-3} , van't Hoff factor = 1), 41 %
 267 succinic acid ($C_6O_4H_6$, density = 1572 kg m^{-3} , van't Hoff factor = 3), and 41 % fulvic
 268 acid ($C_{33}H_{32}O_{19}$, density = 1500 kg m^{-3} , van't Hoff factor = 5) based on a simplification
 269 of observed chemical composition. This mixture is adopted to represent aerosol chemical
 270 composition in this study. In this study, aerosol-radiation interactions, which are the
 271 effect of aerosol on radiation via the reflection, scattering and absorption of shortwave
 272 and longwave radiation by aerosol before its activation, are not considered. This is
 273 partially motivated by the fact that the mixture includes chemical components that absorb
 274 solar radiation insignificantly as compared to strong radiation absorbers such as black
 275 carbon. Based on the AERONET observation, in this study, the tri-modal log-normal
 276 distribution is assumed for the size distribution of background aerosol as exemplified in
 277 Figure 3. Stated differently, it is assumed that the size distribution of background aerosol
 278 at all grid points and time steps has size distribution parameters or the shape of
 279 distribution that is identical to that in Figure 3. The assumed shape of the size distribution
 280 of background aerosol is obtained by averaging size distribution parameters (i.e., modal
 281 radius and standard deviation of each of nuclei, accumulation and coarse modes, and the
 282 partition of aerosol number among those modes) over the AERONET sites and the MCS
 283 period. With these assumption and adoption, PM_{10} is converted to background aerosol
 284 number concentrations. Figures 4a and 4b show example spatial distributions of
 285 background aerosol number concentrations at the surface in Domain 3 (which covers the
 286 Seoul area), which are applied to the control run and represented by black contours.
 287 These distributions in Figures 4a and 4b are calculated based on the surface observation
 288 in Domain 3. Blue contours in Figures 4a and 4b surround areas with observed heavy
 289 precipitation on which this study focuses. In this study, when a precipitation rate at the
 290 surface is 60 mm hr^{-1} or above, precipitation is considered heavy precipitation. There is
 291 no one universal designated rate (of precipitation) above which precipitation is
 292 considered heavy precipitation and the designated rate varies among countries. 60 mm

Deleted: Since

Deleted: , we assume that the mixture does not absorb solar radiation and thus do not simulate the solar absorption of aerosol and attendant effects on stability.

Deleted:

299 hr^{-1} as a precipitation rate is around the upper end of the variation. Those blue contours
300 are further discussed below in Results. Purple lines in Figures 4a and 4b mark the eastern
301 part of where there is substantial transition from high-value aerosol concentrations to
302 low-value aerosol concentrations. In this transition part, there is reduction in aerosol
303 concentrations by more than a factor of 10 from $\sim 9000 \text{ cm}^{-3}$ to $\sim 700 \text{ cm}^{-3}$.

Formatted: Font: (Asian) 맑은 고딕

304 In clouds, aerosol size distributions evolve with sinks and sources, which include
305 advection and droplet nucleation (Fan et al., 2009). Aerosol activation is calculated
306 according to the Köhler theory, i.e., aerosol particles with radii exceeding a critical value
307 at a grid point are activated to become droplets based on predicted supersaturation, and
308 the corresponding bins of the aerosol spectra are emptied. After activation, aerosol mass
309 is transported within hydrometeors by collision-coalescence and removed from the
310 atmosphere once hydrometeors that contain aerosols reach the surface. It is assumed that
311 in the planetary boundary layer (PBL), background aerosol concentrations do not vary
312 with height but above the PBL, background aerosol concentrations reduce exponentially
313 with height. It is also assumed that in non-cloudy areas, aerosol size and spatial
314 distributions are set to follow background counterparts. In other words, once clouds
315 disappear completely at any grid points, aerosol size distributions and number
316 concentrations at those points recover to background counterparts. This assumption has
317 been used by numerous CSRM studies and proven to simulate overall aerosol properties
318 and their impacts on clouds and precipitation reasonably well (Morrison and Grabowski,
319 2011; Lebo and Morrison, 2014; Lee et al., 2016). This assumption indicates that we do
320 not consider the effects of clouds and associated convective and turbulent mixing on the
321 properties of background aerosol. Also, above-explained prescription of those properties
322 (e.g., number concentration, size distribution, and chemical composition) indicates that
323 this study does not take aerosol physical and chemical processes into account. This
324 enables the confident isolation of the sole effects of given background aerosol on clouds
325 and precipitation in the Seoul area, which has not been understood well, by excluding
326 those aerosol processes and cloud effects on background aerosol.

327

328 **3.3 Additional runs**

329

330 As seen in Figures 4a and 4b at 19:00 and 20:00 LST July 27th 2011, there is a large
331 variability of background aerosol concentrations in the Seoul area. This variability is
332 generated by contrast between the high aerosol concentrations in the western part of the
333 domain where aerosol concentration is greater than 1500 cm^{-3} , and the low aerosol
334 concentrations in the eastern part of the domain where aerosol concentration is $\sim 700 \text{ cm}^{-3}$
335 or less. As mentioned above, this study focuses on the effect of the spatial variability and
336 loading (or concentrations) of aerosol on precipitation. To better identify and elucidate
337 the effect, the control run is repeated but with above-mentioned contrast that is reduced.
338 To reduce contrast, over the whole simulation period, the concentrations of background
339 aerosol in the western part of the domain are reduced by a factor of 2, while those in the
340 eastern part do not change. This means that the reduction in the variability accompanies
341 that in aerosol concentrations, which enables us to examine both the effects of the
342 variability and those of concentrations. Note that high and low aerosol concentrations on
343 the left (or western) side and the right (or eastern) side of the domain, respectively, are
344 maintained throughout the whole simulation period, although the location of the
345 boundary between those sides changes with time. Here, in the process of the reduction in
346 contrast, no changes are made for aerosol chemical compositions and size distributions in
347 both parts of the domain. As examples, the spatial distribution of background aerosol
348 concentrations at the surface with reduced contrast at 19:00 and 20:00 LST July 27th 2011
349 is shown in Figures 4c and 4d, respectively. With reduced contrast and concentrations,
350 the variability and concentrations of aerosol are lower in this repeated run than in the
351 control run. The repeated simulation has “low” variability and concentrations of “aerosol”
352 as compared to the control run and thus is referred to as the low-aerosol run.
353 Comparisons between the control run and the low-aerosol run give us a chance to better
354 understand roles played by the spatial variability and loading of aerosol in the spatial
355 distribution of precipitation which involves torrential rain.

356 In addition to the control run and the low-aerosol run, there are more simulations that
357 are performed to better understand the effect of aerosol on precipitation here. To isolate
358 the effects of aerosol concentrations on precipitation from those of aerosol spatial
359 variability or vice versa, the control run and the low-aerosol run are repeated with
360 homogeneous spatial distributions of aerosol. These homogeneous spatial distributions

361 mean that there is no contrast in aerosol number concentrations between the western part
362 of the domain and the eastern part, and aerosol number concentrations do not vary over
363 the domain. The repeated simulations are referred to as the control-homoge run and the
364 low-aerosol-homoge run. The analyses of model results below indicate that differences in
365 precipitation between the control run and the low-aerosol run are closely linked to cloud-
366 liquid evaporative cooling and to elucidate this linkage, the control run and the low-
367 aerosol run are repeated again by turning off cooling from cloud-liquid evaporation.
368 These repeated simulations are referred to as the control-noevp run and the low-aerosol-
369 noevp run. While a detailed description of those repeated simulations is given in Section
370 4.3, a brief description is given in Table 1.

371

372 **4. Results**

373

374 In this study, analyses of results are performed only in the Seoul area (or Domain 3)
375 where the 500-m resolution is applied. Hence, in the following, the description of the
376 simulation results and their analyses are all only over Domain 3, unless otherwise stated.

377

378 **4.1 Meteorological fields, microphysics and precipitation**

379

380 **4.1.1 Meteorological fields and cumulative precipitation**

381

382 Figure 5 shows the observed and simulated vertical profiles of potential temperature,
383 water-vapor mass density, u-wind speed, and v-wind speed which represent
384 meteorological fields. Radiosonde data as observation data are averaged over observation
385 sites in the domain and the simulation period, while simulated meteorological fields are
386 averaged over the domain and the simulation period to obtain the profiles. Positive
387 (negative) u-wind speed represents eastward (westward) wind speed, while positive
388 (negative) v-wind speed represents northward (southward) wind speed. Comparisons
389 between the observed profiles and the simulated counterparts show that overall
390 differences between them are within ~ 10% of observed values. Hence, with confidence,

391 it can be considered that the simulation of meteorological fields is performed reasonably
392 well.

393 The area-mean precipitation rate at the surface smoothed over 3 hours for the control
394 run and the low-aerosol run is depicted by solid lines in Figure 6. Dotted lines in Figure 6
395 depict the precipitation rate for the repeated control run and low-aerosol run and will be
396 discussed in Section 4.3. The simulated precipitation rate in the control run follows the
397 observed counterpart well, which demonstrates that simulations perform reasonably well.
398 Here, observed precipitation is obtained from measurement by rain gauges that are parts
399 of the automatic weather system (AWS) at the surface. The AWS has a spatial resolution
400 of ~ 3 km. Also, the temporal evolution of the mean precipitation rate in the control run is
401 very similar to that in the low-aerosol run. Associated with this similarity, the averaged
402 cumulative precipitation over the domain at the last time step for the control run is 154.7
403 mm, which is just ~ 3 % greater than 150.2 mm for the low-aerosol run.

404

405 **4.1.2 Precipitation fields and frequency distributions**

406

407 Figures 7a, 7b and 7c show frequency distributions of precipitation rates that are
408 collected over all of time steps and all of grid points at the surface in the simulations. In
409 Figure 7, solid lines represent frequency distributions for the control run and the low-
410 aerosol run, while dashed lines represent those for the repeated control run and low-
411 aerosol run which will be described in Section 4.3. Figures 7a, 7d, 7g, 7j, and 7m show
412 frequency distributions only for the control run and the low-aerosol run. The other panels
413 in Figure 7 are supposed to show distributions only for the repeated control run and low
414 aerosol run, however, for comparisons between the control run, the low-aerosol run, and
415 the repeated runs, the control run and the low-aerosol run are displayed as well in those
416 panels.

417 In Figures 7a, 7b, and 7c, frequency distributions of observed precipitation rates that
418 are interpolated to grid points and time steps in the simulations are also shown. The
419 observed maximum precipitation rate is ~ 180 mm hr^{-1} , which is similar to that in the
420 control run. Also, observed frequency distribution is consistent well with the simulated
421 counterpart in the control run, although it appears that particularly for heavy precipitation

422 with rates above 60 mm hr^{-1} , the simulated frequency is underestimated as compared to
423 the observed counterpart. The overall difference in frequency distributions between
424 observation and the control run is much smaller than those between the control run and
425 the low-aerosol run. Hence, we assume that the difference between observation and the
426 control run is considered negligible as compared to that between the runs. Based on this,
427 when it comes to a discussion about the difference between the control run and the low-
428 aerosol run, results in the control run can be assumed to be benchmark results against
429 which the effect of decreases in the spatial variability and concentrations of aerosol on
430 results in the low-aerosol run can be assessed.

431 While we do not see a large difference in cumulative precipitation between the
432 control run (154.7 mm) and the low-aerosol run (150.2 mm), the frequency distribution of
433 precipitation rates shows distinctively different features between the control run and the
434 low-aerosol run (Figure 7a). For precipitation with rates above 60 mm hr^{-1} or heavy
435 precipitation, cumulative frequency is $\sim 60\%$ higher for the control run. For certain
436 ranges of precipitation rates above 60 mm hr^{-1} , there are increases in cumulative
437 frequency by a factor of as much as ~ 10 to ~ 100 . Moreover, for precipitation rates above
438 120 mm hr^{-1} , while there is the presence of precipitation in the control run, there is no
439 precipitation in the low-aerosol run. Hence, we see that there are significant increases in
440 the frequency of heavy precipitation in the control run as compared to that in the low-
441 aerosol run.

442 Figure 8 shows spatial distributions of precipitation rates at the surface. Purple lines
443 in Figure 8 mark the eastern part of where there is substantial transition from high-value
444 aerosol concentrations to low-value aerosol concentrations as in Figure 4. In this
445 transition part, as explained in Figure 4, there is reduction in aerosol concentrations by
446 more than a factor of 10. Figures 8a and 8b show those distributions at 17:00 LST July
447 27th 2011 corresponding to initial stages of precipitating system in the control run and the
448 low-aerosol run, respectively. At 17:00 LST, there is a small area of precipitation around
449 the northwest corner of the domain in both the control run and the low-aerosol run. This
450 implies that a small cloud system develops around the northwest corner of the domain at
451 17:00 LST. The size of the system and its precipitation area grow with time and at 19:00
452 LST, the size is much larger (Figures 8c and 8d). The maximum precipitation rate reaches

453 ~100 mm hr⁻¹ when time progresses to 19:00 LST (Figure 7d). Heavy precipitation is
454 concentrated in a specific area (surrounded by the green rectangle) in both of the runs
455 (Figures 8c and 8d). The green rectangle surrounds a specific area where more than 90 %
456 of the whole events of heavy precipitation (over the domain) with rates above 60 mm hr⁻¹
457 occur in each of the runs at 19:00 LST. Since heavy precipitation starts to form around
458 19:00 LST, the green rectangle starts to be identified around 19:00 LST. Contrast in
459 precipitation between the green rectangle and the other areas in the domain generates an
460 inhomogeneity in the spatial distribution of precipitation. The location of the specific area
461 in the control run is consistent well with the location of heavy precipitation in observation
462 as seen in comparisons between Figures 4a, 8c, and 9a. Figure 9a shows the blue contour,
463 which surrounds areas with observed heavy precipitation in Figure 4a, and the green
464 rectangle, which surrounds the specific area where more than 90 % of the whole events of
465 heavy precipitation occur in Figure 8c. In Figure 9a, the purple line, which marks the
466 transition part where there is the substantial transition in aerosol concentrations in Figure
467 4a, is also shown. The good consistency between the locations demonstrates that the
468 simulation of the spatial distribution of heavy precipitation is performed reasonably well.
469 Between 17:00 LST and 19:00 LST, we do not see significant differences in the
470 frequency distribution of precipitation rates, particularly in heavy precipitation with rates
471 above 60 mm hr⁻¹ between the control run and the low-aerosol run (Figure 7d).

472 By 20:00 LST, the maximum rate of torrential rain reaches ~130 mm hr⁻¹ for the
473 control run and ~110 mm hr⁻¹ for the low-aerosol run (Figure 7g). Associated with this,
474 between 19:00 and 20:00 LST, significant differences in frequency distributions,
475 particularly for heavy precipitation between the control run and the low-aerosol run, start
476 to appear (Figure 7g). At 20:00 LST as seen in Figure 8e and in the previous hours, in the
477 control run, more than 90 % of heavy precipitation events are concentrated in a specific
478 area that is surrounded by the green rectangle. Note that only in this specific area,
479 extremely heavy precipitation with rates above 100 mm hr⁻¹ occurs. In the low-aerosol
480 run, the extremely heavy precipitation with rates above 100 mm hr⁻¹ also occurs only in a
481 particular area, which is surrounded by the green rectangle, at 20:00 LST (Figure 8f). At
482 20:00 LST, as seen in Figure 4b, observation shows that there are five spots of heavy
483 precipitation. The location of the largest spot where most of heavy precipitation events

484 occur is similar to that of the specific area that is surrounded by the green rectangle in the
485 control run as seen in comparisons between Figures 4b, 8e and 9b. Figure 9b shows the
486 blue contour and the purple line in Figure 4b and the green rectangle in Figure 8e. This
487 again demonstrates that the simulation of the spatial distribution of heavy precipitation is
488 performed with fairly good confidence.

489 The system propagates eastwards after 20:00 LST in a way that its easternmost part
490 is closer to the east boundary of the domain as seen in comparisons between Figure 8e
491 (Figure 8f) and Figure 8g (Figure 8h) for the control (low-aerosol) run. As seen in Figure
492 8g and in the previous hours, for the control run, more than 90 % of heavy precipitation
493 events are concentrated in a specific area (surrounded by the green rectangle) at 23:00
494 LST. However, in the low-aerosol run, heavy precipitation is not concentrated in a
495 specific area at 23:00 LST. Unlike the green rectangle in the control run at 23:00 LST,
496 the green rectangle at 23:00 LST in the low-aerosol run surrounds an area where ~50 %
497 of heavy precipitation events are located, although the rectangle surrounds the largest
498 area with heavy precipitation among heavy precipitation areas in the low-aerosol run. For
499 a period between 20:00 and 23:00 LST as compared to that between 19:00 and 20:00
500 LST, the maximum precipitation rate rises up to $\sim 180 \text{ mm hr}^{-1}$ in the control run,
501 however, in the low-aerosol run, the maximum precipitation rate stays at $\sim 120 \text{ mm hr}^{-1}$
502 (Figures 7g and 7j). Hence, there is the presence of precipitation rates between ~ 120 and
503 $\sim 180 \text{ mm hr}^{-1}$ in the control run, while there is their absence in the low-aerosol run for the
504 period between 20:00 and 23:00 LST. This reflects that increases in the frequency of
505 torrential rain, which are induced by increases in the spatial variability and loading of
506 aerosol, enhance, as the system evolves from its initial stage before 20:00 LST to mature
507 stage between 20:00 and 23:00 LST.

508 Of interest is that the green rectangle is included in an area which is surrounded by
509 the purple line in all panels with different times in Figure 8 and further discussion for this
510 matter is provided in Section 4.2. After 23:00 LST July 27th 2011, the precipitating
511 system enters its decaying stage. Figure 7m shows precipitation-rate frequency in the
512 control run and the low-aerosol run for a period between 04:00 and 05:00 LST July 28th
513 2011. As seen in Figure 7m, with the progress of the decaying stage, the maximum

514 precipitation rate reduces down to $\sim 25 \text{ mm hr}^{-1}$ as an indication that heavy precipitation
515 disappears and the system is nearly at the end of its life cycle.

516

517 **4.2 Dynamics**

518

519 **4.2.1 Convergence**

520

521 For the examination of condensation which is the main source of precipitation,
522 convergence fields at the surface, where updrafts that produce condensation are
523 originated, are obtained and the column-averaged condensation rates are superimposed
524 on them. Other processes such as deposition and freezing produce the mass of solid
525 hydrometeors and act as sources of precipitation, however, their contribution to
526 precipitation is \sim one order of magnitude smaller than that by condensation in the control
527 run and the low-aerosol run. Hence, here, among sources of precipitation, we focus on
528 condensation. Convergence and condensation fields are again superimposed on shaded
529 precipitation fields as shown in Figure 10. In Figure 10, convergence and condensation
530 fields are represented by white and yellow contours, respectively. When it comes to the
531 convergence field in the green rectangle in Figure 10, which starts to be formed around
532 19:00 LST and is composed of convergence lines, the field in the rectangle in the control
533 run is stronger than that in the low-aerosol run. The averaged intensity of the
534 convergence field over an area with non-zero convergence in the green rectangle and
535 over the simulation period is 0.013 s^{-1} in the control run, while the averaged intensity is
536 0.007 s^{-1} in the low-aerosol run. The convergence field in the green rectangle is strongest
537 among convergence lines over the whole domain and, associated with this, stronger
538 updrafts and greater condensation develop over that field in the green rectangle than in
539 the other lines over the whole domain in each of the runs.

540 Figure 11 shows horizontal distributions of wind-vector field (arrows) superimposed
541 upon fields of convergence, condensation, and precipitation. In general, particularly from
542 19:00 LST on, in the area with high-value aerosol concentrations to the west of the strong
543 convergence field (surrounded by the green rectangle), there are greater horizontal wind
544 speeds than in the area with low-value aerosol concentrations to the east of the strong

Deleted: zero in

546 convergence field in the control run. As seen in comparisons between the location of the
547 rectangle and that of the purple line, which mark the transition zone for aerosol
548 concentrations, the area to the west of the rectangle has higher aerosol concentrations
549 than that to the east. In that area with high-value aerosol concentrations, there is greater
550 cloud-liquid evaporation occurring than in that area with low-value aerosol
551 concentrations in the control run as shown in Figure 12a. Figure 12a shows the vertical
552 distribution of the time- and domain-averaged cloud-liquid and rain evaporation rates
553 over each of the areas to the west and east of the strong convergence field, which is
554 surrounded by the green rectangle, and over the period between 17:00 and 19:00 LST for
555 the control run and the low-aerosol run. For the calculation of the averaged values in
556 Figure 12, the area to the west (east) of the strong convergence field is set to include all
557 parts of the north-south direction, which is the y-direction, and the vertical domains but a
558 portion of the east-west direction domain, which is the x-direction domain that extends
559 from the western boundary of Domain 3 to 90 km where the western boundary of the
560 green rectangle at 19:00 LST is located (from 110 km where the eastern boundary of the
561 green rectangle at 19:00 LST is located to the eastern boundary of Domain 3) in Domain
562 3 for the control run. For the low-aerosol run, the area to the west (east) of the strong
563 convergence field is identical to that in the control run except for the fact that the area
564 includes a portion of the x-direction domain that extends from the western boundary of
565 Domain 3 to 70 km where the western boundary of the green rectangle at 19:00 LST is
566 located (from 90 km where the eastern boundary of the green rectangle at 19:00 LST is
567 located to the eastern boundary of Domain 3) in Domain 3.

568 High-value aerosol concentrations reduce autoconversion and in turn, increase
569 cloud liquid as a source of evaporation and thus, increase cloud-liquid evaporation as
570 compared to low-value aerosol concentrations. In addition, high-value aerosol
571 concentrations produce high-value cloud droplet number concentration and the associated
572 high-value surface areas of droplets. The surface of droplets is where condensation
573 occurs and as shown by Lee et al. (2009) and a recent study by Fan et al. (2018), the
574 high-value surface areas cause higher-value condensation as compared to the situation
575 with low-value aerosol concentrations that lead to lower-value condensation. The
576 averaged condensation rate over the above-mentioned area to the west (east) of the strong

Deleted:

578 convergence field and over the period between 17:00 and 19:00 LST is $1.28 (0.97) \text{ g m}^{-3}$
579 h^{-1} in the control run. This further increases cloud liquid (as a source of evaporation) and
580 thus its evaporation in the area with high-value aerosol concentrations. Also, with high-
581 value aerosol concentrations, there is an increase in the surface-to-volume ratio of cloud
582 droplets and this increases evaporation efficiency and thus, cloud-liquid evaporation as
583 compared to the situation with low-value aerosol concentrations. However, mainly due to
584 an increase in the size of raindrops and their associated decrease in the surface-to-volume
585 ratio, which are induced by high-value aerosol concentrations, rain evaporation reduces
586 as compared to the situation with low-value aerosol concentrations as also shown in van
587 den Heever et al. (2011). Increases in cloud-liquid evaporation in turn enhance negative
588 buoyancy, which induces stronger downdrafts in the area with high-value aerosol
589 concentrations than in the area with low-value aerosol concentrations in the control run
590 particularly between 17:00 LST and 19:00 LST as seen in Figure 12b. Sublimation and
591 melting also enhance negative buoyancy, however, their contribution is ~one order of
592 magnitude smaller than the contribution by cloud-liquid evaporation. Hence, here, we
593 focus on cloud-liquid evaporation. Figure 12b shows the vertical distribution of the time-
594 and domain-averaged downdraft mass fluxes over each of the areas to the west and east
595 of the strong convergence field (surrounded by the green rectangle) for the control run
596 and the low-aerosol run over the period between 17:00 and 19:00 LST. Previous studies
597 have shown that aerosol-induced increases in cloud-liquid evaporation are closely linked
598 to the enhancement of the intensity of downdrafts (Lee et al., 2008a, b; Lee et al., 2013;
599 Lee, 2017). Cloud liquid or droplets in downdrafts move together with downdrafts, thus,
600 when downdrafts descend, cloud liquid descends while being included in downdrafts.
601 Cloud liquid in the descending downdrafts evaporates. More evaporation of cloud liquid
602 provides greater negative buoyancy to downdrafts so that they accelerate more (Byers
603 and Braham, 1949; Grenzi and Nese, 2001).

604 After reaching the near-surface altitudes below ~3 km, in the control run, stronger
605 downdrafts spread out as stronger outflow or horizontal movement as seen in the area
606 with high-value aerosol concentrations as compared to those in the area with low-value
607 aerosol concentrations around 19:00 LST in Figure 11c. The outflow in the area with
608 high-value aerosol concentrations accelerates, due to evaporation on its path, as it moves

Formatted: Superscript

Formatted: Superscript

609 southeastwards from the northern and western boundaries of the domain. The outflow
610 accelerates until it collides with surrounding air that has weaker horizontal movement in
611 the area with low-value aerosol concentrations. This collision mainly occurs in the places
612 where the transition between high-value aerosol concentrations and low-value aerosol
613 concentrations is located (surrounded by the purple line) as seen in Figure 11c. This
614 collision creates the strong convergence field around 19:00 LST, which is surrounded by
615 the green rectangle in those places in the control run as seen in Figure 11c. Hence, most
616 of the strong convergence field (surrounded by the green rectangle) is included in the
617 transition zone between high-value and low-value aerosol concentrations (which is
618 surrounded by the purple line) in the control run (Figure 11c). The strong convergence
619 field in the green rectangle generates a large amount of condensation and cloud liquid and
620 this large amount of cloud liquid produces not only heavy precipitation but also high-
621 degree evaporation. Then, high-degree evaporation in turn contributes to the occurrence
622 of a stronger convergence field in the green rectangle, which establishes feedbacks
623 between the convergence field, condensation, heavy precipitation, and evaporation. This
624 enables the intensification of downdrafts and horizontal wind to the west of the green-
625 rectangle convergence field, the convergence field, and the increases in the heavy
626 precipitation with time, while the green-rectangle convergence field is advected
627 eastwards in the control run as seen in Figures 7g, 7j, 11e and 11g. As seen in Figures
628 11e and 11g, even after 19:00 LST, the green-rectangle convergence field stays within
629 the transition zone between the high-value and low-value aerosol concentrations (which
630 is surrounded by the purple line) during its eastward advection. This indicates that above-
631 explained collision between strong outflow and surrounding weak wind, which is
632 essential for the formation of the green-rectangle convergence field, continuously occurs
633 in the transition zone even after 19:00 LST.

634 Note that, associated with aerosol concentrations in the western part of the domain,
635 which are two times greater in the control run than in the low-aerosol run, there are two
636 times greater differences in aerosol concentrations between the area with high-value
637 aerosol concentrations and that with low-value aerosol concentrations in the control run
638 than in the low-aerosol run. This leads to a two times greater transition in aerosol
639 concentrations, particularly in the transition zone surrounded by the purple line in the

640 control run than in the low-aerosol run (Figure 4). Associated with this, there are greater
641 reduction in autoconversion and increases in cloud liquid and surface-to-volume ratio of
642 cloud droplets in the area with high-value aerosol concentrations in the control run than
643 in the low-aerosol run. Then, there are greater evaporation, intensity of downdrafts,
644 associated outflow and its acceleration during its southeastward movement around the
645 surface in that area in the control run than in the low-aerosol run (Figures 11 and 12).
646 This means that there is stronger collision between outflow and the surrounding air in the
647 control run than in the low-aerosol run, and stronger collision forms the strong
648 convergence field (in the green rectangle) which is much more intense in the control run
649 than in the low-aerosol run as seen in Figures 10 and 11. Over this much more intense
650 convergence field, there is the formation of stronger updrafts that are able to form
651 stronger convection, which is in turn able to produce more events of heavy precipitation
652 in the control run than in the low-aerosol run (Figure 7). The more intense strong
653 convergence field in the green rectangle establishes stronger feedbacks between the
654 convergence field, condensation, heavy precipitation, and evaporation in the control run
655 than in the low-aerosol run. Hence, differences in intensity of the green-rectangle
656 convergence field and in the heavy precipitation between the runs get greater as time
657 progresses (Figures 7, 10 and 11).

658

659 **4.3 Sensitivity tests**

660

661 **4.3.1 Evaporative cooling**

662

663 It is discussed that cloud-liquid evaporative cooling plays an important role in the
664 formation of the strong convergence field where most of heavy precipitation occurs
665 (surrounded by the green rectangle) in the control run. To confirm this role, we repeat the
666 control run and the low-aerosol run with cooling from cloud-liquid evaporation turned off
667 and cooling from rain evaporation left on. The repeated control run and the low-aerosol
668 run are referred to as the control-noevp run and the low-aerosol-noevp run, respectively.
669 In these repeated runs, cloud-liquid mass reduces due to cloud-liquid evaporation,
670 although cloud-liquid evaporation does not affect temperature.

671 The temporal evolution of precipitation rates in the control-noevp run and the low-
672 aerosol-noevp run is similar to that in the control run and the low-aerosol run (Figure 6a).
673 However, due to the absence of cloud-liquid evaporative cooling, there is no formation of
674 the strong outflow and convergence field (as seen in wind field and the green rectangle in
675 the control run and the low-aerosol run) in these repeated runs as shown in Figures 13a
676 and 13b. Figures 13a and 13b show wind-vector and convergence fields at the surface
677 over the whole domain in the control-noevp run and the low-aerosol-noevp run,
678 respectively, at 23:00 LST which corresponds to the mature stage of the system. Note that
679 the strong convergence field is clearly distinguishable in its intensity and length from any
680 other convergence lines in each of the control run and the low-aerosol run as seen in
681 Figures 10 and 11. However, there is no field in each of the repeated runs that is
682 distinguishable in their intensity and length from other lines as seen in Figures 13a and
683 13b. This leads to the situation where there is no particular convergence field in the
684 control-noevp run that produces much more events of heavy precipitation than those in
685 the low-aerosol-noevp run. As seen in Figures 7h and 7k, associated with this, differences
686 in the frequency of heavy precipitation with rates above 60 mm hr^{-1} between the repeated
687 runs are much smaller than those between the control run and the low-aerosol run
688 particularly for the period between 19:00 LST and 23:00 LST, although the control-
689 noevp run shows the greater frequency of heavy precipitation than the low-aerosol-noevp
690 run. This results in much smaller differences in heavy precipitation between the repeated
691 runs than between the control run and the low-aerosol run for the whole simulation period
692 as seen in Figure 7b. This demonstrates that cloud-liquid evaporative cooling and its
693 differences between the control run and the low-aerosol run play a key role in much more
694 events of heavy precipitation in the control run than in the low-aerosol run.

695

696 **4.3.2 Variability of aerosol concentrations**

697

698 Remind that between the control run and the low-aerosol run, there are changes not only
699 in the spatial variability of aerosol concentrations but also in aerosol concentrations. This
700 means that differences between those runs are caused not only by changes in the
701 variability but also by those in aerosol concentrations. Although there have been many

702 studies on the effects of changes in aerosol concentrations on heavy precipitation, studies
703 on those effects of changes in the variability have been rare. Motivated by this, as a
704 preliminary step to the understanding of those effects of changes in the variability, here,
705 we attempt to isolate the effects of changes in the variability on heavy precipitation from
706 those in aerosol concentrations or vice versa. For this purpose, the control run and the
707 low-aerosol run are repeated with homogeneous spatial distributions of background
708 aerosol concentrations. These repeated runs are referred to as the control-homoge run and
709 the low-aerosol-homoge run. In the control-homoge run (low-aerosol-homoge run),
710 aerosol concentrations over the domain are fixed at one value, which is the domain-
711 averaged concentration of the background aerosol in the control run (the low-aerosol run),
712 at each time step. Hence, in the control-homoge run and the low-aerosol-homoge run, the
713 variability (or contrast) in the spatial distribution of aerosol concentrations between the
714 area with high-value aerosol concentrations and that with low-value aerosol
715 concentrations is removed, which achieves homogeneous spatial distributions.

716 The temporal evolution of precipitation rates in the control-homoge run and the low-
717 aerosol-homoge run is similar to that in the control run and the low-aerosol run (Figure
718 6b). However, with the homogeneity in the spatial distribution of aerosol concentrations,
719 there is no formation of strong outflow and thus, strong convergence field that is
720 distinguishable from any other convergence lines in the control-homoge run and low-
721 aerosol-homoge run as seen in Figures 13c and 13d. Figures 13c and 13d show wind-
722 vector and convergence fields over the whole domain at 23:00 LST in the control-
723 homoge run and the low-aerosol-homoge run, respectively. In the absence of the
724 variability between the area with high-value aerosol concentrations and that with low-
725 value aerosol concentrations, there are no differences in evaporative cooling between
726 those areas and thus, there are no strong outflow and thus, strong convergence field
727 which is distinguishable from any other lines.

728 Comparisons between the control run and the control-homoge run (the low-aerosol
729 run and the low-aerosol-homoge run) isolate the effects of the variability on heavy
730 precipitation from those of aerosol concentrations whose averaged value is set at an
731 identical value at each time step in the runs. Due to the absence of the variability in the
732 spatial distribution of aerosol concentrations and the associated strong convergence field,

733 the frequency of heavy precipitation in the control-homoge run and in the low-aerosol-
734 homoge run is, on average, just ~18 and ~13 % of that in the control run and in the low-
735 aerosol run, respectively, for the whole simulation period (Figure 7c). Hence, the
736 presence of the variability alone (in the absence of changes in aerosol concentrations)
737 increases the number of the heavy-precipitation events by a factor of ~ 5 or ~ 10. This
738 presence alone also results in a substantial increase in the maximum precipitation rate in
739 the control run and the low-aerosol run as compared to the repeated runs. Between the
740 low-aerosol run and the low-aerosol-homoge run, the increase is from 80 mm hr⁻¹ in the
741 low-aerosol-homoge run to 120 mm hr⁻¹ in the low-aerosol run, while between the control
742 run and the control-homoge run, the increase is significant and from 90 mm hr⁻¹ in the
743 control-homoge run to 180 mm hr⁻¹ in the control run (Figure 7c). Here, we see that even
744 without the effects of changes in aerosol concentrations, the presence of the variability
745 alone is able to cause the significant enhancement of heavy precipitation in terms of its
746 frequency and maximum value.

747 Remember that there is an identical domain-averaged background aerosol
748 concentration at each time step between the control run and the control-homoge run and
749 between the low-aerosol run and the low-aerosol-homoge run. Hence, changes in the
750 averaged aerosol concentration between the control-homoge run and the low-aerosol-
751 homoge run are identical to those between the control run and the low-aerosol run. With
752 these identical changes in the averaged aerosol concentration, between the control run
753 and the low-aerosol run, there are additional changes in the variability of aerosol
754 distributions. There is the larger frequency of heavy precipitation in the control-homoge
755 run than in the low-aerosol-homoge run (Figure 7c). However, as mentioned above, there
756 is no strong convergence field which is distinguishable from any other lines in the
757 control-homoge run as seen in Figure 13c. Associated with this, differences in the
758 frequency of heavy precipitation between the control-homoge run and the low-aerosol-
759 homoge run are much smaller than those between the control run and the low-aerosol run
760 particularly during the period between 19:00 LST and 23:00 LST, as seen in Figures 7i
761 and 7l. This results in a situation where differences in the frequency of heavy
762 precipitation between the control-homoge run and the low-aerosol-homoge run are, on
763 average, just ~15 % of those between the control run and the low-aerosol run for the

764 whole simulation period (Figure 7c). With identical changes in the averaged aerosol
765 concentration between a pair of the control run and the low-aerosol run and a pair of the
766 control-homoge run and the low-aerosol-homoge run, this demonstrates that additional
767 changes in the variability of aerosol distributions play a much more important role in
768 aerosol-induced increases in the occurrence of heavy precipitation than changes in the
769 averaged aerosol concentrations.

770

771 **5. Summary and conclusion**

772

773 This study examines how aerosol affects heavy precipitation in an urban conurbation area.
774 For this examination, a case that involves an MCS and torrential rain over the
775 conurbation area which centers in Seoul, Korea is simulated. This case has large spatial
776 variability in aerosol concentrations which involves high-value aerosol concentrations in
777 the western part of the domain and low-value aerosol concentrations in the eastern part of
778 the domain.

779 It is well-known that increases in aerosol concentrations reduce autoconversion and
780 increase cloud liquid as a source of evaporation, which enhance evaporation and
781 associated cooling. Hence, high-value aerosol concentrations in the western part of the
782 domain cause high-value evaporative cooling rates, while low-value aerosol
783 concentrations in the eastern part of the domain cause low-value evaporative cooling
784 rates. Greater evaporative cooling produces greater negative buoyancy and more intense
785 downdrafts in the western part than in the eastern part. More intense downdrafts then
786 turn into stronger outflow over the western part that collides with surrounding air over the
787 eastern part to form a strong convergence field along the boundary between those parts.
788 Over this strong convergence field, most of heavy precipitation forms. When contrast in
789 aerosol concentrations between the western and eastern parts, which represents the spatial
790 variability in aerosol concentrations, reduces together with reducing aerosol
791 concentrations over the western part, differences in evaporative cooling and outflow
792 between those parts decrease substantially. This results in a much weaker convergence
793 field along the boundary, which is followed by much less occurrences of heavy-
794 precipitation events as compared to those with greater contrast. It is found that the

795 changing variability has much more impacts on heavy precipitation than the changing
796 aerosol loading.

797 Studies (e.g., Niyogi et al., 2006; Thielen et al., 2000) have shown that at the edge of
798 a metropolitan area, due to stark contrast in the surface roughness (representing the
799 surface property) between the area and surrounding rural areas, there are enhanced
800 convergence and updrafts. The urban heat island (UHI) effect, which is associated with
801 the surface property in metropolitan areas, also results in enhanced convergence and
802 updrafts at the edge of the area (Ryu et al., 2013; Schmid and Niyogi, 2017). In addition,
803 a metropolitan area has stronger and more aerosol sources than surrounding rural areas,
804 hence, contrast in aerosol concentrations at the edge of a metropolitan area or at the
805 urban/rural boundary, which is characterized by contrast in the surface property between
806 the urban and rural areas, is unlikely to be rare. This study suggests that in case there is
807 this type of contrast in aerosol properties such as aerosol concentration at the boundary,
808 there can be enhanced convergence and updrafts at the edge of a metropolitan area.
809 Hence, this study suggests that urban/rural contrast in aerosol should be considered as an
810 additional factor (in addition to contrast in the surface roughness and the UHI effect) to
811 understand the enhancement of convergence and updrafts at the edge of a metropolitan
812 area.

813 It should be noted that urban surface properties, which are represented by the
814 roughness and control the UHI effect, and their contrast with the rural surface properties
815 do not vary significantly with respect to time and space as compared to the variation of
816 aerosol properties. Hence, the location of the urban/rural boundary does not change with
817 time and space significantly. However, in contrast to this, aerosol properties vary
818 substantially with respect to time and space and thus the location of boundary between
819 high-aerosol concentrations and low-aerosol concentrations vary with respect to time and
820 space substantially. For example, in a place such as a large-scale industrial complex
821 within an urban area away from an urban boundary, there can be an increase in aerosol
822 concentrations and thus high aerosol concentrations. These high aerosol concentrations
823 can advect, as exemplified in the case adopted in this study, and a boundary between a
824 place with low-aerosol concentrations and a place with high aerosol concentrations can
825 vary spatiotemporally within the urban area. This indicates that the boundary between the

826 place with high-aerosol concentrations and that with low-aerosol concentrations does not
827 necessarily have to be co-located with the urban/rural boundary which is characterized by
828 contrast in the surface property between urban and rural areas and whose location does
829 not change much with respect to time and space. Demonstrating this, in this study, the
830 high-aerosol/low-aerosol boundary, which is, for example, surrounded by the purple line
831 in Figures 4a and 4b, is not co-located with the urban/rural boundary but located in the
832 middle of the Seoul area. Considering that on the high-aerosol/low-aerosol boundary,
833 heavy precipitation is concentrated in this study, a spatiotemporal variation of the
834 boundary leads to a spatiotemporal variation of heavy precipitation within an urban area
835 as shown in this study. Hence, while previous theories on urban heavy precipitation can
836 explain heavy precipitation on urban/rural boundaries (characterized by the surface-
837 property contrast) and are not able to explain heavy precipitation in various locations
838 within an urban area, the findings in this study elucidate a mechanism behind heavy
839 precipitation in various locations in an urban area and thus give us more comprehensive
840 understanding of torrential rain in urban areas.

841 There are numerous factors that control the spatial distribution of updrafts and
842 associated condensation. Note that changes in this distribution induce those in the spatial
843 distribution of precipitation that may involve the generation and the enhancement of
844 torrential rain. One of the factors is found to be increasing aerosol concentrations by
845 previous studies (e.g., Khain et al., 2005; Seifert and Beheng, 2006; van den Heever and
846 Contton, 2007; Tao et al., 2007; Storer et al., 2010; Tao et al., 2012; Lee and Feingold,
847 2013; Lee et al., 2017). These previous studies have found that increasing aerosol
848 concentrations can alter the vertical and horizontal gradient of latent heating and cooling
849 by altering the spatial distributions of freezing, evaporation, and condensation. This
850 alteration leads to that in updrafts, cloud cells, and precipitation, which involves the
851 generation and the enhancement of torrential rain. However, these studies have focused
852 only on increasing aerosol concentrations and assumed that background aerosol
853 concentrations are spatially distributed in a homogeneous fashion, hence, have not
854 considered the effect of the spatial variability in aerosol on the spatial distribution of
855 latent-heat processes, cloud dynamics, and precipitation. For example, the previous
856 studies have found that aerosol-induced localized changes in evaporation for individual

857 cloud cells can create subsequent localized changes in the horizontal gradient of latent
858 cooling and temperature in and around individual cloud cells. Note that each of these
859 individual localized changes is limited to each of individual localized areas in and around
860 each of individual cloud cells. These changes lead to the generation and the enhancement
861 of torrential rain in and around individual cloud cells. It is found that increasing spatial
862 variability in aerosol concentrations also increases the gradient of evaporation and
863 temperature. These changes lead to increases in the occurrence of heavy precipitation in a
864 specific area which is along the high-aerosol/low-aerosol boundary and is not limited to a
865 localized area in and around a cloud cell. It is demonstrated that increasing variability
866 plays a much more important role in aerosol-induced increases in the occurrence of heavy
867 precipitation than increases in aerosol concentrations with their homogeneous spatial
868 distributions.

869 As mentioned, observed aerosol particles include components which do not absorb
870 radiation significantly, hence, the aerosol absorption of radiation is not considered in this
871 study. However, ammonium sulfate and organic compound, which are observed to
872 comprise aerosol here, reflect and scatter radiation, although these reflection and
873 scattering are not considered in this study. The reflection and scattering of particularly
874 solar radiation by aerosol decrease solar radiation that reaches the surface and thus
875 surface fluxes. Higher aerosol concentrations in the western part of the domain can cause
876 more reflection and scattering of solar radiation by aerosol than in the eastern part. This
877 can reduce surface fluxes, the associated convection intensity, condensation, and
878 transportation of cloud liquid to unsaturated areas by convective motion in the western
879 part more than in the eastern part. As a result, there can be reduction in the contrast in
880 evaporative cooling between the parts as compared to the contrast with no consideration
881 of the reflection and scattering. This can lower the intensity and frequency of heavy
882 precipitation by diminishing the contrast in wind field between the parts. However, the
883 simulated intensity and frequency of heavy precipitation with no consideration of the
884 reflection and scattering by aerosol are not that deviant from observed counterparts. This
885 indicates that the effect of the reflection and scattering by aerosol, and associated changes
886 in surface fluxes on heavy precipitation is likely to be insignificant in reality. This is
887 likely to be due to the fact that once deep clouds with high-value cloud fraction and cloud

888 optical depth form, the effect of aerosol on radiation is taken over by that of clouds on
889 radiation, which leads to a situation where aerosol effects on radiation become negligible
890 as compared to cloud effects on radiation.

891

892

893

894

895

896

897

898

899

900

901

902

903

904

905

906

907

908

909

910

911

912

913

914

915

916

917

918

919 **Acknowledgements**

920

921 This study is supported by the United States National Oceanic and Atmospheric
922 Administration (Grant NOAA-NWS-NWSPO-2015-2004117), and the National Strategic
923 Project-Fine particle of the National Research Foundation of Korea (NRF) funded by the
924 Ministry of Science and ICT (MSIT), the Ministry of Environment (ME), and the
925 Ministry of Health and Welfare (MOHW) (NRF-2017M3D8A1092022). This research is
926 supported by Basic Science Research Program through the National Research Foundation
927 of Korea (NRF) funded by the Ministry of Education(2018R1A6A1A08025520).

928

929

930

931

932

933

934

935

936

937

938

939

940

941

942

943

944

945

946

947

948

949

Deleted: This work is supported by Priority Research Centers Program through the National Research Foundation of Korea (NRF) funded by the Ministry of Science and ICT (2018R1A6A1A08025520).

955 **References**

- 956
- 957 Bouvette, T., Lambert, J. L., and Bedient, P. B.: Revised rainfall frequency analysis for
 958 Houston, *J. Hydraul. Div. Proc. Amer. Soc. Civil Eng.* 108, 515–528, 1982.
- 959 Brown, A., Milton, S., Cullen, M., Golding, B., Mitchell, J., and Shelly, A.: Unified
 960 modeling and prediction of weather and climate: A 25-year journey, *Bull. Am*
 961 *Meteorol. Soc.* 93, 1865–1877, 2012.
- 962 Burian, S. J., and Shepherd, J. M.: Effects of urbanization on the diurnal rainfall pattern
 963 in Houston: Hydrological processes, *Rainfall Hydrol. Proc.* 19, 1089–1103, 2005.
- 964 Byers, H. R., and Braham, R. R.: The thunderstorm, U. S. Weather Bur., Washington, D.
 965 C., 287 pp, 1949.
- 966 Chen, F., and Dudhia, J.: Coupling an advanced land-surface hydrology model with the
 967 Penn State-NCAR MM5 modeling system. Part I: Model description and
 968 implementation, *Mon. Wea. Rev.* 129, 569–585, 2001.
- 969 Chen S., et al.: Urbanization effect on precipitation over the Pearl River Delta based on
 970 CMORPH data, *Adv. Clim. Chang. Res.* 6, 16-22, 2015.
- 971 Dhar, O. N., and Nandergji, S.: The zones of severe rainstorm activity over India, *Int. J.*
 972 *Climatol.* 13, 301-311, 1993.
- 973 Diem, J. E., and Brown, D. P.: Anthropogenic impacts on summer precipitation in central
 974 Arizona, *U. S. A. Prof. Geogr.* 55, 343–355, 2003.
- 975 [Fan, J., Rosenfeld, D., Zhang, Y., et al.: Substantial convection and precipitation
 976 enhancements by ultrafine aerosol particles, *Science*, 359, 411-418,
 977 doi:10.1126/science.aan8461, 2018.](#)
- 978 Fan, J., Yuan, T., Comstock, J. M., et al.: Dominant role by vertical wind shear in
 979 regulating aerosol effects on deep convective clouds, *J. Geophys. Res.* 114,
 980 doi:10.1029/2009JD012352, 2009.
- 981 Fouquart, Y., and Bonnel, B.: Computation of solar heating of the Earth's atmosphere: a
 982 new parameterization, *Beitr. Phys. Atmos.* 53, 35-62, 1980.
- 983 Fujibe, F.: Long-term surface wind changes in the Tokyo metropolitan area in the
 984 afternoon of sunny days in the warm season, *J. Meteor. Soc. Japan* 81, 141–149,
 985 2003.
- Deleted:** (1982) ...vised rainfall frequency (...)
- Deleted:** (2012) ...nified modeling and (...)
- Deleted:** (2005) ...ffects of urbanization on t(...)
- Deleted:** ... (1949) ...he thunderstorm, U. S. (...)
- Deleted:** (2001) ...oupling an advanced land(...)
- Deleted:** (2015) ...rbanization effect on (...)
- Deleted:** (1993) ...he zones of severe rainstor(...)
- Deleted:** (2003) ...nthropogenic impacts on (...)
- Deleted:** ... Yuan, T., Comstock, , ... M., et (...)
- Deleted:** ¶ (...)
- Deleted:** (2003) ...ong-term surface wind (...)

- 1044 Gilliland, E. K., and Rowe, C. M.: A comparison of cumulus parameterization schemes in
 1045 the WRF model. Proceedings of the 87th AMS annual meeting: available at
 1046 <https://ams.confex.com/ams/pdfpapers/120591.pdf>, 2007.
- 1047 Grenzi, L. M., and Nese, J. M.: A world of weather: fundamentals of meteorology: a text/
 1048 laboratory manual, Kendall/Hunt Publishing Company, 2001.
- 1049 Holben, B. N., Tanré, D., Smirnov, et al.: An emerging ground-based aerosol
 1050 climatology: Aerosol optical depth from AERONET. *J. Geophys. Res.*, 106, 12067–
 1051 12097, 2001.
- 1052 Hwang, S.-O., and Lee, D.-K.: A study on the relationship between heavy rainfalls and
 1053 associated low-level jets in the Korean peninsula. *J. Korean Meteorol. Soc.*, 29,
 1054 133–146, 1993.
- 1055 Kain, J. S., and Fritsch, J. M.: A one dimensional entraining/detraining plume model and
 1056 its application in convective parameterization. *J. Atmos. Sci.*, 47, 2784-2802, 1990.
- 1057 Kain, J. S., and Fritsch, J. M.: Convective parameterization for mesoscale models: The
 1058 Kain-Fritsch scheme. The representation of cumulus convection in numerical
 1059 models. *Meteor. Monogr.*, No. 24, Amer. Meteor. Soc., 165-170, 1993.
- 1060 Khain, A., BenMoshe, N., and Pokrovsky, A.: Factors determining the impact of aerosols
 1061 on surface precipitation from clouds: Attempt of classification. *J. Atmos. Sci.*, 65,
 1062 1721-1748, 2008.
- 1063 Khain, A., Pokrovsky, A., Rosenfeld, D., Blahak, U., and Ryzhkov, A.: The role of CCN
 1064 in precipitation and hail in a mid-latitude storm as seen in simulations using a
 1065 spectral (bin) microphysics model in a 2D dynamic frame, *Atmos. Res.*, 99, 129–
 1066 146, 2011.
- 1067 Khain, A., Rosenfeld, D., and Pokrovsky, A.: Aerosol impact on the dynamics and
 1068 microphysics of deep convective clouds. *Quart. J. Roy. Meteor. Soc.*, 131, 2639-
 1069 266, 2005.
- 1070 Korea Meteorological Administration: Heavy rainfall events top 10, KMA registered
 1071 Pub., No. 11-136000-000833-01, Seoul, Korea, 48 p, 2011.
- 1072 Lebo, Z.: A numerical investigation of the potential effects of aerosol-induced warming
 1073 and updraft width and slope on updraft intensity in deep convective clouds. *J.*
 1074 *Atmos. Sci.* doi:10.1175/JAS-D-16-0368.1, 2017.

Deleted: (2007)

Deleted: .

Deleted: (2001)

Deleted: .

Deleted: (2001)

Deleted: .

Deleted: .

Deleted: .

Deleted: (1993)

Deleted: .

Deleted: .

Deleted: .

Deleted: (1990)

Deleted: ¶

Deleted: .

Deleted: .

Deleted: .

Deleted: .

Deleted: (1993)

Deleted: .

Deleted: .

Deleted: .

Deleted: (2008)

Deleted: .

Deleted: .

Deleted: .

Deleted: .

Deleted: (2011),

Deleted: .

Deleted: .

Deleted: (2005)

Deleted: .

Deleted: .

Deleted: .

Deleted: (2011)

Deleted: .

Deleted: (2017)

Deleted: .

Deleted: .

Deleted: .

Deleted: .

- 1115 Lebo, Z. J., and Morrison, H.: Dynamical effects of aerosol perturbations on simulated
 1116 idealized squall lines, *Mon. Wea. Rev.*, 142, 991-1009, 2014.
- 1117 Lebo, Z. J., and Seinfeld, J. H.: Theoretical basis for convective invigoration due to
 1118 increased aerosol concentration, *Atmos. Chem. Phys.*, 11, 5407-5429, 2011.
- 1119 Lee, D.-K., Kim, H.-R., and Hong, S.-Y.: Heavy rainfall over Korea during 1980-1990.
 1120 Korean J. Atmos. Sci., 1, 32-50, 1998.
- 1121 Lee, S. S., Donner, L. J., Phillips, V. T. J., and Ming, Y.: Examination of aerosol effects
 1122 on precipitation in deep convective clouds during the 1997 ARM summer
 1123 experiment, *Q. J. R. Meteorol. Soc.*, 134, 1201-1220, 2008a.
- 1124 Lee, S. S., Donner, L. J., Phillips, V. T. J., and Ming, Y.: The dependence of aerosol
 1125 effects on clouds and precipitation on cloud-system organization, shear and stability,
 1126 *J. Geophys. Res.*, 113, D16202, 2008b.
- 1127 Lee, S. S., and Feingold, G.: Aerosol effects on the cloud-field properties of tropical
 1128 convective clouds, *Atmos. Chem. Phys.*, 13, 6713-6726, 2013.
- 1129 Lee, S. S., Li, Z., Mok, J., et al.: Interactions between aerosol absorption,
 1130 thermodynamics, dynamics, and microphysics and their impacts on clouds and
 1131 precipitation in a multiple-cloud system, *Clim. Dyn.*,
 1132 <https://doi.org/10.1007/s00382-017-3552-x>, 2017.
- 1133 Lee, S. S., Penner, J. E., and Saleeby, S. M.: Aerosol effects on liquid-water path of thin
 1134 stratocumulus clouds, *J. Geophys. Res.*, 114, D07204, doi:10.1029/2008JD010513,
 1135 2009.
- 1136 Lee, S. S., Kim, B.-G., and Yum, S. S., et al.: Effect of aerosol on evaporation, freezing
 1137 and precipitation in a multiple cloud system, *Clim. Dyn.*, 48, 1069-1087, 2016.
- 1138 Li, Z., Niu, F., Fan, J., Liu, Y., Rosenfeld, D., and Ding, Y.: Long-term impacts of
 1139 aerosols on the vertical development of clouds and precipitation, *Nat. Geosci.*, 4,
 1140 888-894, 2011.
- 1141 Mannan, Md. A., Chowdhury, Md. A., and Karmakar, S.: Application of NWP model in
 1142 prediction of heavy rainfall in Bangladesh, *Pac. Sci.*, 56, 667-675, 2013.
- 1143 Mladek, et al.: Intercomparison and evaluation of precipitation forecasts for MAP seasons
 1144 1995 and 1996, *Meteorol. Atmos. Phys.*, 72, 111-129, 2000.
- 1145 Mlawer, E. J., Taubman, S. J., Brown, P. D., Iacono, M. J., and Clough, S. A.: RRTM, a

Deleted: (2014) ...ynamical effects of aerosol (...)

Deleted: (2011) ...heoretical basis for convec (...)

Deleted: (1998) ...eavy rainfall over Korea (...)

Deleted: (2008a) ...xamination of aerosol effi (...)

Deleted: (2008b) ...he dependence of aerosol (...)

Deleted: (2013) ...erosol effects on the cloud (...)

Deleted: (2017) ...nteractions between (...)

Deleted: , 2017... 2017.. (...)

Deleted: (2016) ...ffect of aerosol on (...)

Deleted: (2011)

Deleted:Nat. Geosci., 4,...888-894, 2011 (...)

Deleted: (2013) ...pplication of NWP model (...)

Deleted: (2000) ...ntercomparison and (...)

Deleted: (1997)

- 1205 validated correlated-k model for the longwave, *J. Geophys. Res.*, 102, 16663-1668,
 1206 [1997](#).
- 1207 Morrison, H., and Grabowski, W. W.: Cloud-system resolving model simulations of
 1208 aerosol indirect effects on tropical deep convection and its thermodynamic
 1209 environment, *Atmos. Chem. Phys.*, 11, 10503–10523, [2011](#).
- 1210 Niyogi, D., Holt, T., Zhong, S., Pyle, P. C., and Basara, J.: Urban and land surface
 1211 effects on the 30 July 2003 mesoscale convective system event observed in the
 1212 southern Great Plains, *J. Geophys. Res.*, 111, 1–20, [2006](#).
- 1213 Rosenfeld, D., Lohmann, U., Raga, G. B., et al.: Flood or drought, How do aerosols
 1214 affect precipitation? *Science*, 321, 1309-1313, [2008](#).
- 1215 Ryu, Y.-H., Baik, J.-J., and Han, J.-Y.: Daytime urban breeze circulation and its
 1216 interaction with convective cells, *Q. J. R. Meteorol. Soc.*, 139, 401–413, [2013](#).
- 1217 Sauer, V. B., Thomas, W. O., Stricker, V. A., and Wilson, K. V.: Flood characteristics of
 1218 urban watersheds in the United States, United States Geological Survey Water-
 1219 Supply Paper 2207, pp 63, [1984](#).
- 1220 Schmid, P. E., and Niyogi, D.: Modeling urban precipitation modification by spatially
 1221 heterogeneous aerosols, *J. Appl. Meteorol. Climatol.*, [https://doi.org/10.1175/JAMC-](https://doi.org/10.1175/JAMC-D-16-0320.1)
 1222 [D-16-0320.1](https://doi.org/10.1175/JAMC-D-16-0320.1), [2017](#).
- 1223 Seifert, A., and Beheng, K. D.: A two-moment cloud microphysics parameterization for
 1224 mixed-phase clouds. Part 2: Maritime vs. continental deep convective storms,
 1225 *Meteorol. Atmos. Phys.*, 92, 67-82, [2006](#).
- 1226 Shepherd, J. M.: A review of current investigations of urban-induced rainfall and
 1227 recommendations for the future, *Earth Interact.*, 9, 1-27, [2005](#).
- 1228 Storer, R. L., van den Heever, S. C., and Stephens, G. L.: Modeling aerosol impacts on
 1229 convection under differing storm environments, *J. Atmos. Sci.*, 67, 3904-3915, [2010](#).
- 1230 [Seo, K.-H., Son, J. H., Lee, J.-H., and Park, H.-S.: Northern East Asian monsoon
 1231 precipitation revealed by air mass variability and its prediction, *J. Clim.*, 28, 6221-
 1232 6233, 2013.](#)
- 1233 Takahashi, H.: Secular variation in the occurrence property of summertime daily rainfall
 1234 amount in and around the Tokyo metropolitan area (in Japanese with an English
 1235 abstract), *Tenki*, 50, 31–41, [2003](#).

Deleted:
Deleted:
Deleted:
Deleted: (2011)
Deleted:
Deleted:
Deleted: (2006)
Deleted:
Deleted:
Deleted: (2008)
Deleted:
Deleted: (2013)
Deleted:
Deleted:
Deleted: (1984)
Deleted:
Deleted: (2017)
Deleted:
Deleted:
Deleted: (2006)
Deleted:
Deleted:
Deleted: (2005)
Deleted:
Deleted: (2010)
Deleted:
Deleted:
Deleted: Sun J, and Lee T-Y (2002) A numerical study of an intense quasistationary convection ...
Deleted: Sun J, and Lee T-Y (2002) A ...
Deleted: (2003)
Deleted:
Deleted:
Deleted:

- 1287 Tao, W.-K., Chen, J.-P., Li, Z., Wang, C., and Zhang, C.: Impact of aerosols on
 1288 convective clouds and precipitation. *Rev. Geophys.* 50, RG2001, 2012.
- 1289 Tao, W.-K., Li, X., Khain, A., Matsui, T., Lang, S., and Simpson, J.: Role of atmospheric
 1290 aerosol concentration on deep convective precipitation: Cloud-resolving model
 1291 simulations. *J. Geophys. Res.* 112, D24S18, 2007.
- 1292 Thielen, J., Wobrock, W., Gadian, A., Mestayer, P., and Creutin, J.-D.: The possible
 1293 influence of urban surfaces on rainfall development: a sensitivity study in 2D in the
 1294 meso- γ -scale. *Atmos. Res.* 54, 15–39, 2000.
- 1295 United Nations, Department of Economic and Social Affairs, Population Division: World
 1296 urbanization prospects: The 2014 Revision, (ST/ESA/SER.A/366),
 1297 <https://esa.un.org/unpd/wup>, 2015.
- 1298 van den Heever, S. C., Carrió, G. G., Cotton, W. R., DeMott, P. J., and Prenni, A.
 1299 J.: Impacts of nucleating aerosol on florida storms. part I: Mesoscale simulations. *J.*
 1300 *Atmos. Sci.* 63, 1752–1775, 2006.
- 1301 van den Heever, S. C., and Cotton, W. R.: Urban aerosol impacts on downwind
 1302 convective storms. *J. Appl. Meteorol. Clim.* 46, 828–850, 2007.
- 1303 van den Heever, S. C., Stephens, G. L., and Wood, N. B.: Aerosol indirect effects on
 1304 tropical convection characteristics under conditions of radiative-convective
 1305 equilibrium. *J. Atmos. Sci.* 68, 699–718, 2011.
- 1306 Wang, H., Skamarock, W. C., and Feingold, G.: Evaluation of scalar advection schemes
 1307 in the Advanced Research WRF model using large-eddy simulations of aerosol-
 1308 cloud interactions. *Mon. Wea. Rev.* 137, 2547–2558, 2009.
- 1309 Wang, Y., Zhang, R., Saravanan, R.: Asian pollution climatically modulates mid-latitude
 1310 cyclones following hierarchical modelling and observational analysis. *Nature*
 1311 *Comm.* 5, 3098, 2014.
- 1312 Yeh, H.-C., and Chen, G. T.-J.: Case study of an unusually heavy rain event over eastern
 1313 Taiwan during the Mei-Yu Season. *Mon. Wea. Rev.* 132, 320–337, 2004.
- 1314
 1315
 1316
 1317
 1318
 1319

Deleted: (2012)

Deleted: .

Deleted: .

Deleted: .

Deleted: (2007)

Deleted: .

Deleted: .

Deleted: .

Deleted: .

Deleted: (2000)

Deleted: .

Deleted: .

Deleted: (2015)

Deleted: .

Deleted: (2006)¶

Deleted: .

Deleted: .

Deleted: .

Deleted: (2007)

Deleted: .

Deleted: .

Deleted: .

Deleted: (2011)

Deleted: .

Deleted: .

Deleted: (2009)

Deleted: .

Deleted: .

Deleted: .

Deleted: (2014)

Deleted: .

Deleted: .

Deleted: .

Deleted: (2004)

Deleted: .

Deleted: .

Deleted: .

Deleted: .

1358 | **FIGURE CAPTIONS**

1359
1360

1361 Figure 1. 850 hPa wind (m s^{-1} ; arrows), geopotential height (m; contours), and equivalent
1362 potential temperature (K; shaded) at 21:00 LST July 26th 2011 over Northeast Asia. The
1363 rectangle in the Korean Peninsula in the panel marks Domain 3 that is explained in
1364 Section 3.2 and shown in Figure 2.

1365
1366

1367 Figure 2. Triple-nested domains used in the CSRM simulations. The boundary of the
1368 figure itself is that of Domain 1, while the rectangles marked by “d02” and “d03”
1369 represent the boundary of Domain 2 and Domain 3, respectively. The dotted line
1370 represents the boundary of Seoul and terrain heights are contoured every 250 m.

1371

1372 Figure 3. Aerosol size distribution at the surface. N represents aerosol number
1373 concentration per unit volume of air and D represents aerosol diameter.

1374

1375 Figure 4. Spatial distributions of background aerosol number concentrations at the
1376 surface (black contours; in “ $\times 10^3 \text{ cm}^{-3}$ ”) and the boundary of each area that has
1377 precipitation rate of 60 mm hr^{-1} or above (blue contours) in Domain 3 at (a) 19:00 LST
1378 and (b) 20:00 LST. Purple lines in panels (a) and (b) mark a part of the domain where
1379 there is a substantial reduction in aerosol number concentrations (see text for the details
1380 of purple lines). Panels (c) and (d) are the same as panels (a) and (b), respectively, but
1381 with reduced contrast in aerosol number concentrations for the low-aerosol run (see text
1382 for the details of reduced contrast).

1383

1384 Figure 5. Vertical distributions of the averaged (a) potential temperature, (b) water vapor
1385 mass density, (c) u-wind speed, and (d) v-wind speed. Positive (negative) u-wind speed
1386 represents eastward (westward) wind speed, while positive (negative) v-wind speed
1387 represents northward (southward) wind speed. Observations are averaged over
1388 observation sites in Domain 3 and the simulation period, while simulations are averaged
1389 over Domain 3 and the simulation period.

Deleted: ¶

¶
¶
¶
¶
¶
¶
¶

1399

1400 Figure 6. Time series of the area-mean precipitation rates at the surface smoothed over 3
1401 hours for the control run, the low-aerosol run, and observation in Domain 3. In panel (a),
1402 the rates in the control-noevp run and the low-aerosol-noevp are additionally shown,
1403 while in panel (b), the rates in the control-homoge run and the low-aerosol-homoge are
1404 additionally shown.

1405

1406 Figure 7. Frequency distributions of the precipitation rates at the surface, which are
1407 collected over the whole domain, for (a), (b), and (c) the whole simulation period, (d), (e),
1408 and (f) a period between 17:00 and 19:00 LST, (g), (h), and (i) a period between 19:00
1409 and 20:00 LST, (j), (k), and (l) a period between 20:00 and 23:00 LST, and (m), (n), and
1410 (o) a period between 04:00 and 05:00 LST. In panels (a), (b), and (c) observed frequency
1411 which is interpolated to the simulation time steps and grid points is also shown.

1412

1413 Figure 8. Spatial distributions of precipitation rates at the surface. Green rectangles mark
1414 areas with heavy precipitation and are described in detail in text. Purple lines mark the
1415 eastern part of where there is substantial transition from high-value aerosol
1416 concentrations to low-value aerosol concentrations as in Figure 4. Panels (a), (c), (e) and
1417 (g) are for the control run, while panels (b), (d), (f) and (h) are for the low-aerosol run.
1418 Panels (a) and (b) are for 17:00 LST, and panels (c) and (d) are for 19:00 LST, while
1419 panels (e) and (f) are for 20:00 LST, and panels (g) and (h) are for 23:00 LST.

1420

1421 Figure 9. Boundary of each area which has the observed surface precipitation rate of 60
1422 mm hr^{-1} or above (blue contours) and a specific area (surrounded by the green rectangle
1423 in the control run and described in text related to Figure 8) where heavy precipitation is
1424 concentrated in the control run in Domain 3 at (a) 19:00 LST and (b) 20:00 LST. Purple
1425 lines are the same as in Figure 8.

1426

1427 Figure 10. Same as Figure 8 but with convergence at the surface (white contours) and the
1428 column-averaged condensation rates (yellow contours) which are superimposed on the
1429 precipitation field. In panels (a) and (b), white contours are at 0.4 and $0.7 \times 10^{-2} \text{ s}^{-1}$ and

1430 yellow contours are at 0.4 and 0.9 g m⁻³ h⁻¹. In panels (c) and (d), white contours are at
1431 0.9 and 1.7 × 10⁻² s⁻¹ and yellow contours are at 0.9 and 1.5 g m⁻³ h⁻¹. In panels (e) and (f),
1432 white contours are at 1.4 and 2.3 × 10⁻² s⁻¹ and yellow contours are at 1.3 and 2.9 g m⁻³ h⁻¹.
1433 In panels (g) and (h), white contours are at 2.1 and 3.5 × 10⁻² s⁻¹ and yellow contours are
1434 at 2.3 and 3.8 g m⁻³ h⁻¹.

1435

1436 Figure 11. Same as Figure 10 but with wind-vector fields (arrows) which are
1437 superimposed on the precipitation, convergence, and condensation fields.

1438

1439 Figure 12. Vertical distributions of the time- and domain-averaged (a) cloud-liquid and
1440 rain evaporation rates and (b) downdraft mass fluxes over each of the areas to the west
1441 and east of the strong convergence field for the control run and the low-aerosol run over a
1442 period between 17:00 and 19:00 LST (see text for details).

1443

1444 Figure 13. Spatial distributions of convergence (red contours) and wind vector (arrows) at
1445 the surface at 23:00 LST. Panels (a), (b), (c), and (d) are for the control-noevp run, the
1446 low-aerosol-noevp run, the control-homoge run, and the low-aerosol-homoge run,
1447 respectively, and contours are at 2.1 and 3.5 × 10⁻² s⁻¹.

1448

1449

1450

1451

1452

1453

1454

1455

1456

1457

1458

1459

1460

Simulations	Contrast in aerosol number concentration	The effect of cloud-liquid evaporation on temperature
Control run	Observed	Present
Low-aerosol run	Reduced by a factor of 2	Present
Control-noevp run	Observed	Absent
Low-aerosol-noevp run	Reduced by a factor of 2	Absent
Control-homoge run	Absent	Present
Low-aerosol-homoge run	Absent	Present

1461

1462 Table 1. Summary of simulations

1463

1464

1465

1466

1467

1468

1469

1470

1471

1472

1473

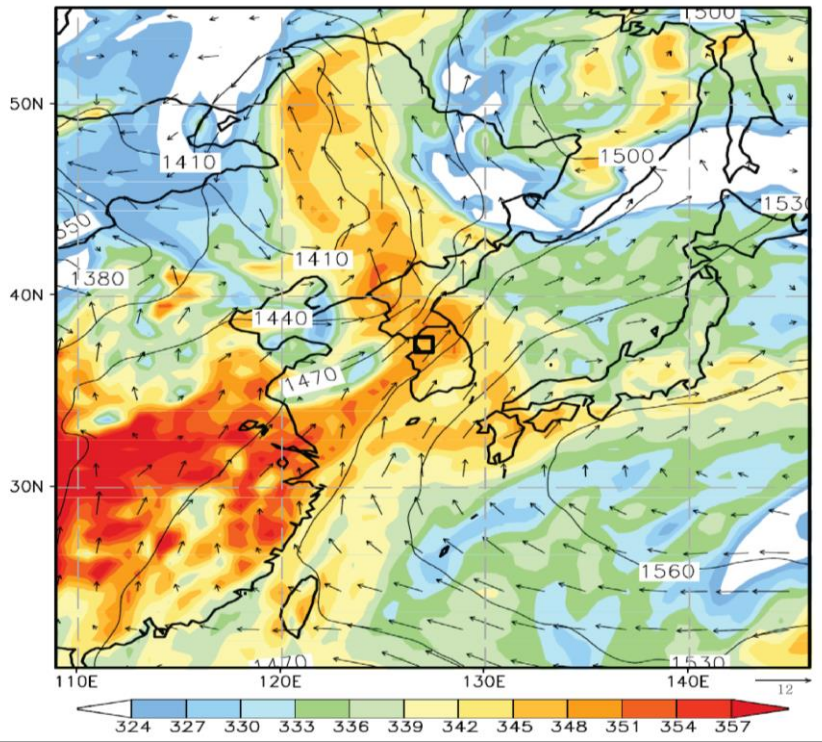
1474

1475

1476

1477

1478

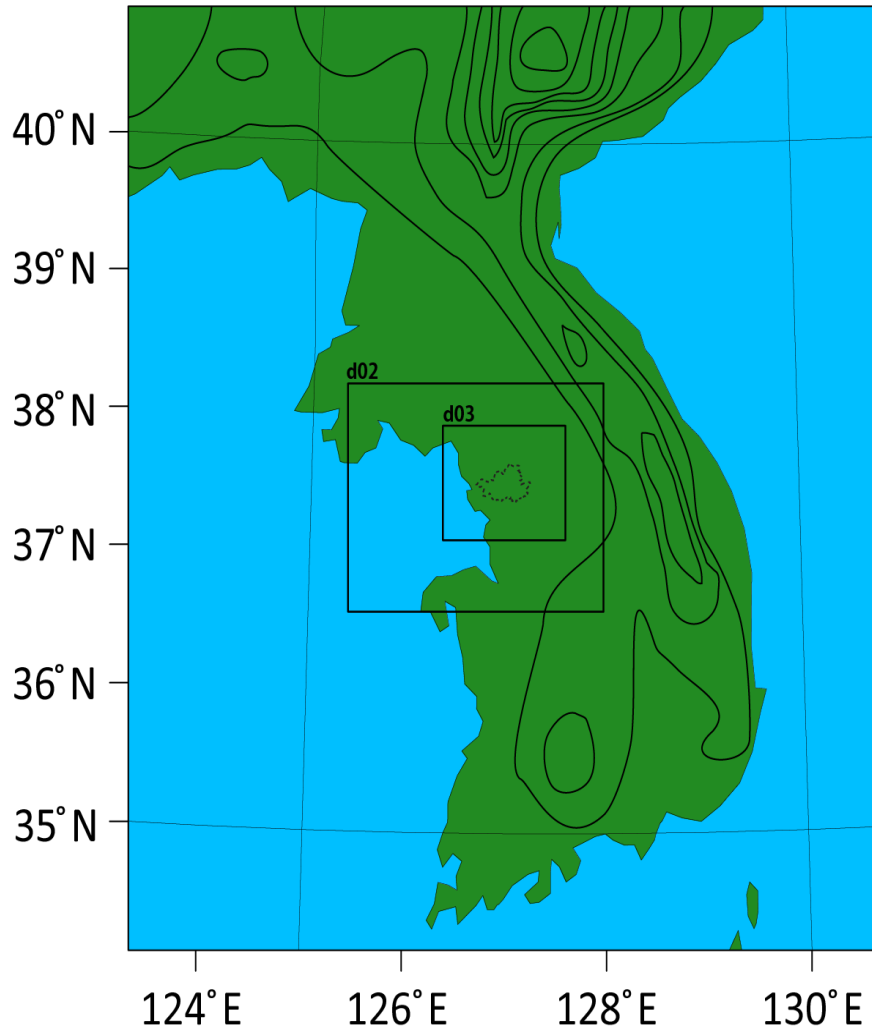


1479

1480

1481

Figure 1



1482

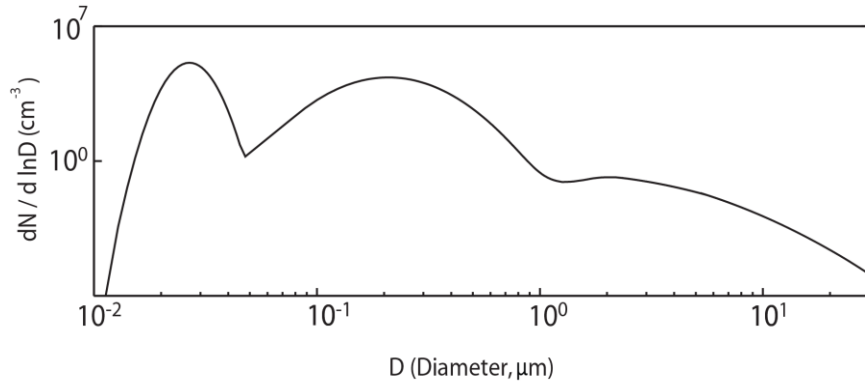
1483

1484

1485

1486

Figure 2



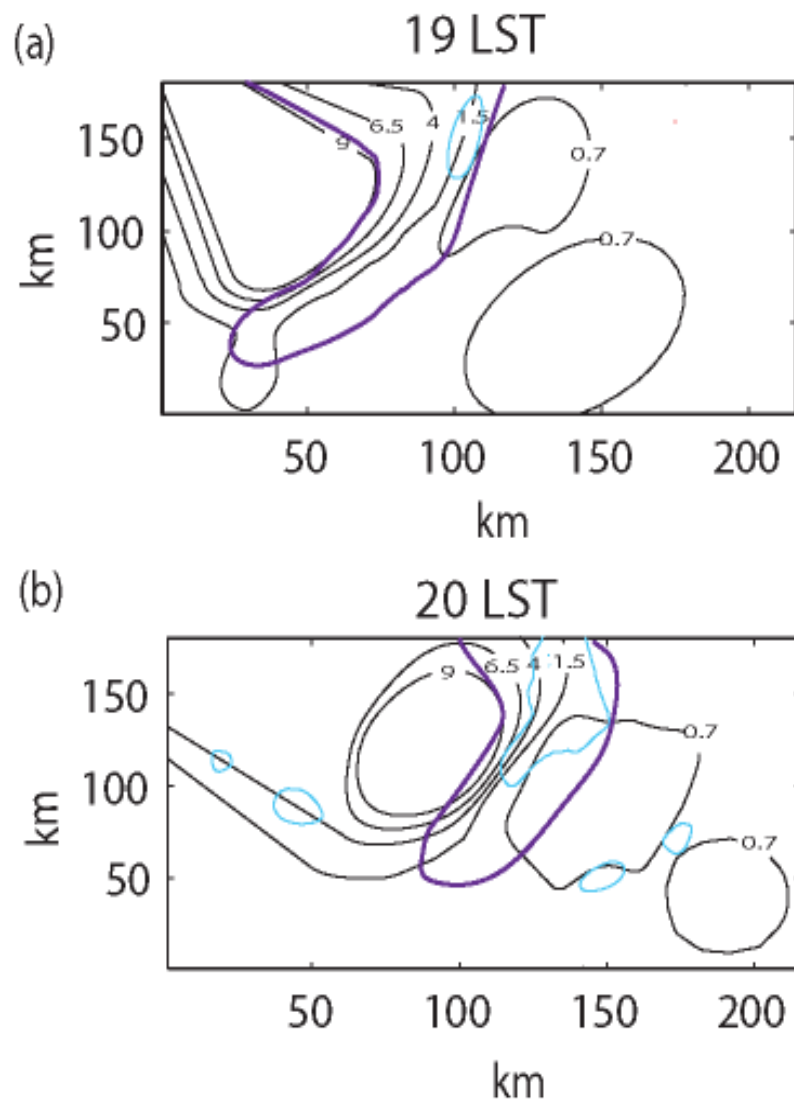
1487

1488

1489

1490

Figure 3

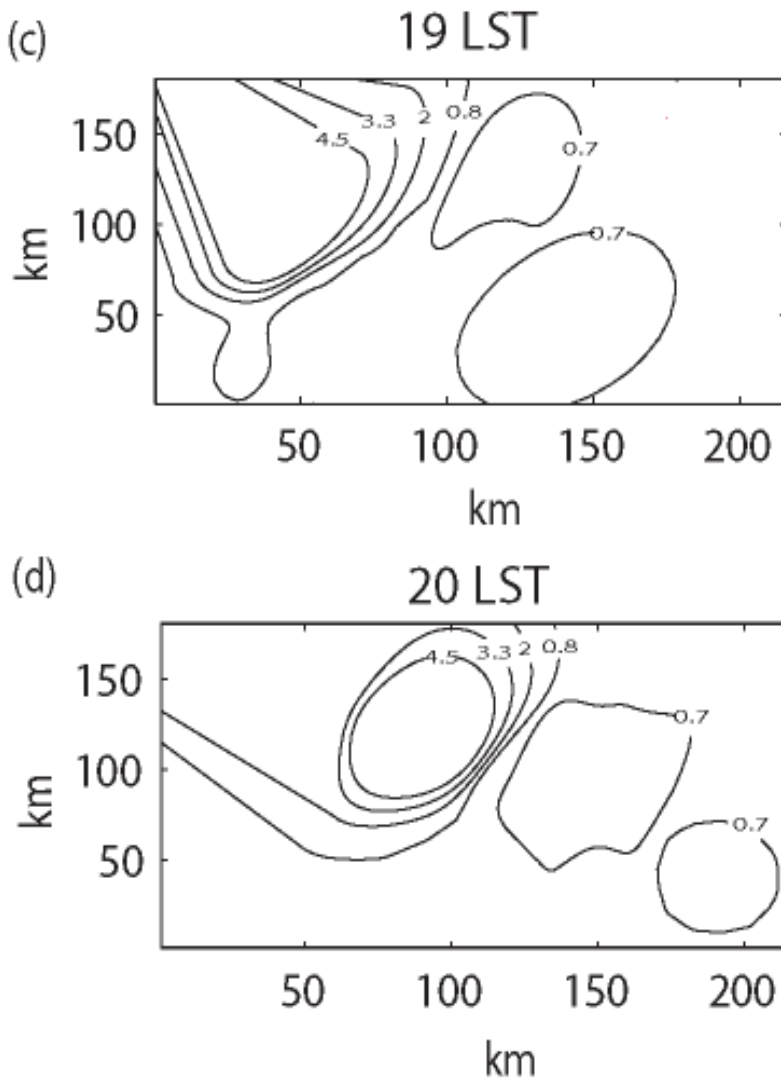


1491

1492

1493

Figure 4



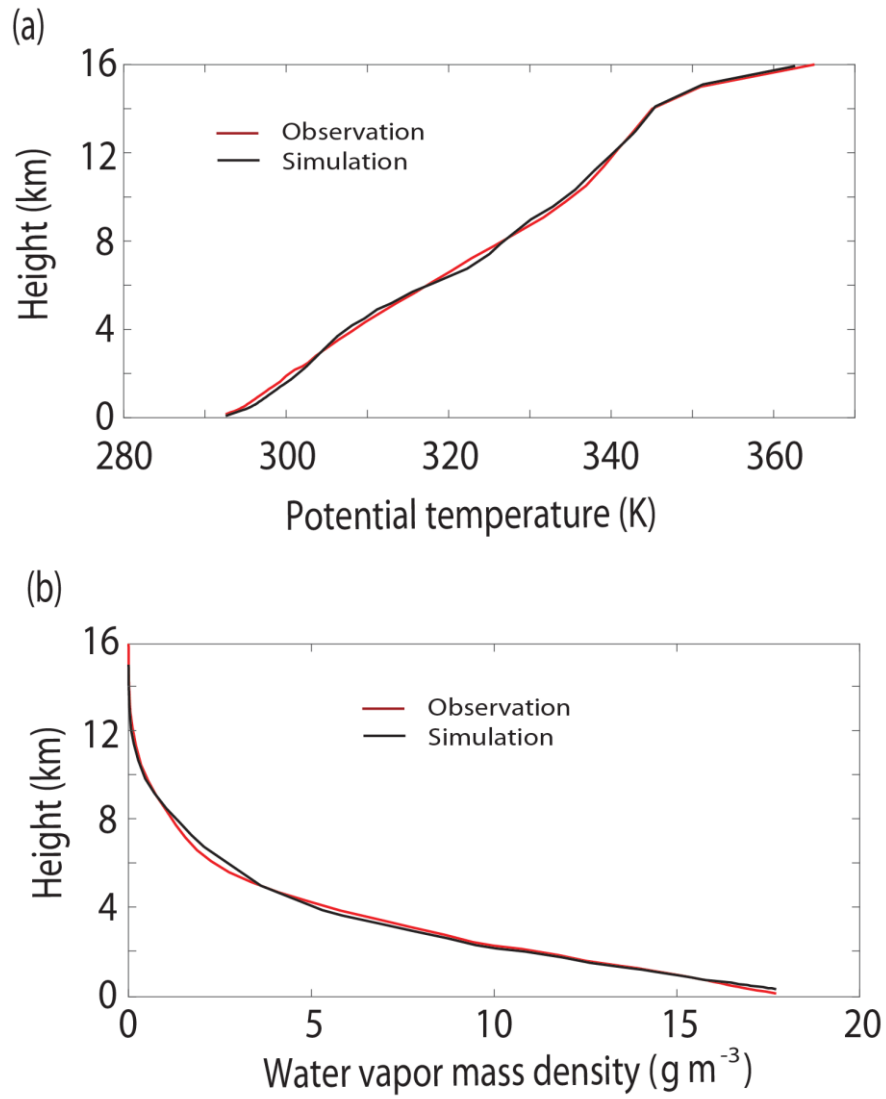
1494

1495

1496

1497

Figure 4



1498

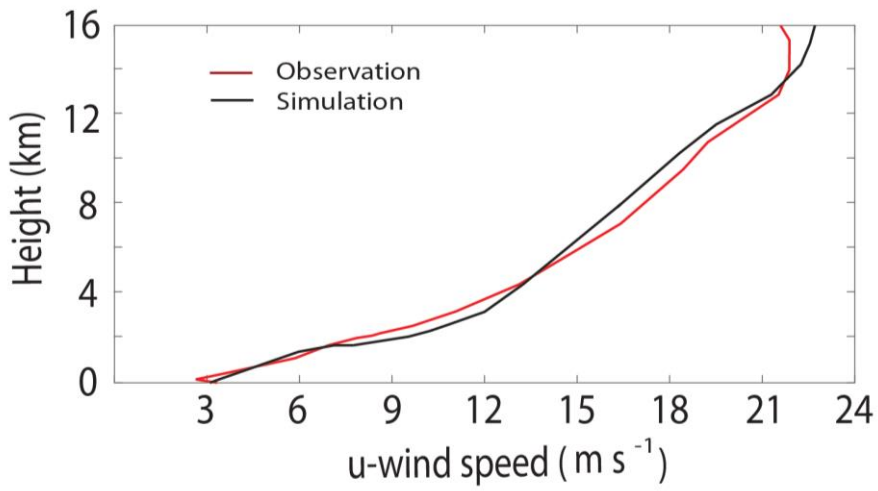
1499

1500

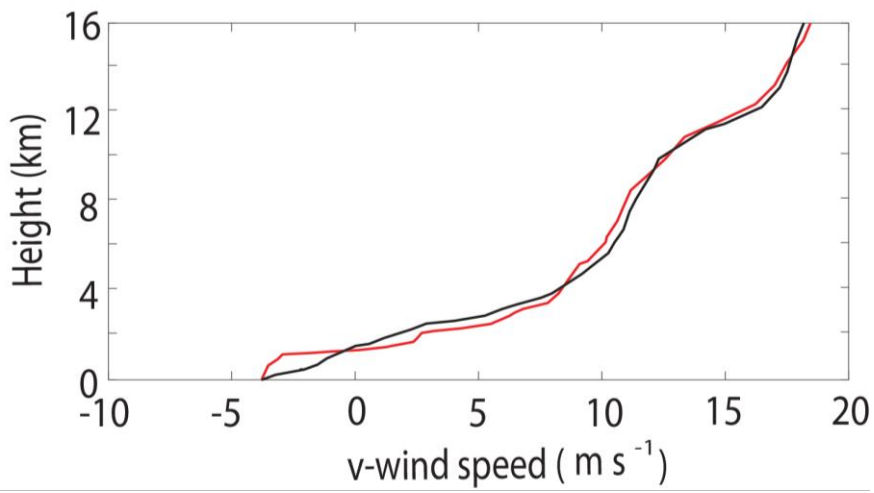
1501

Figure 5

(c)



(d)

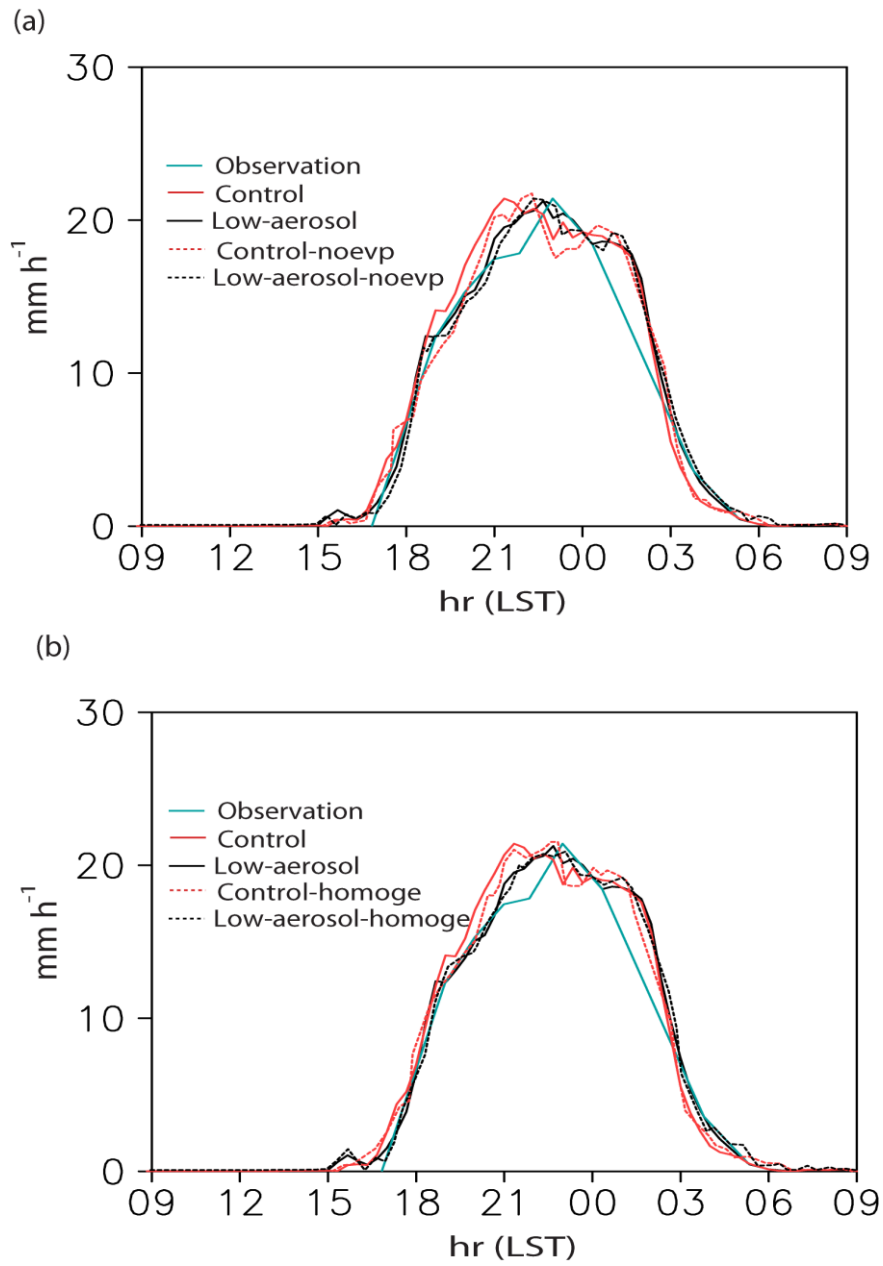


1502

1503

1504

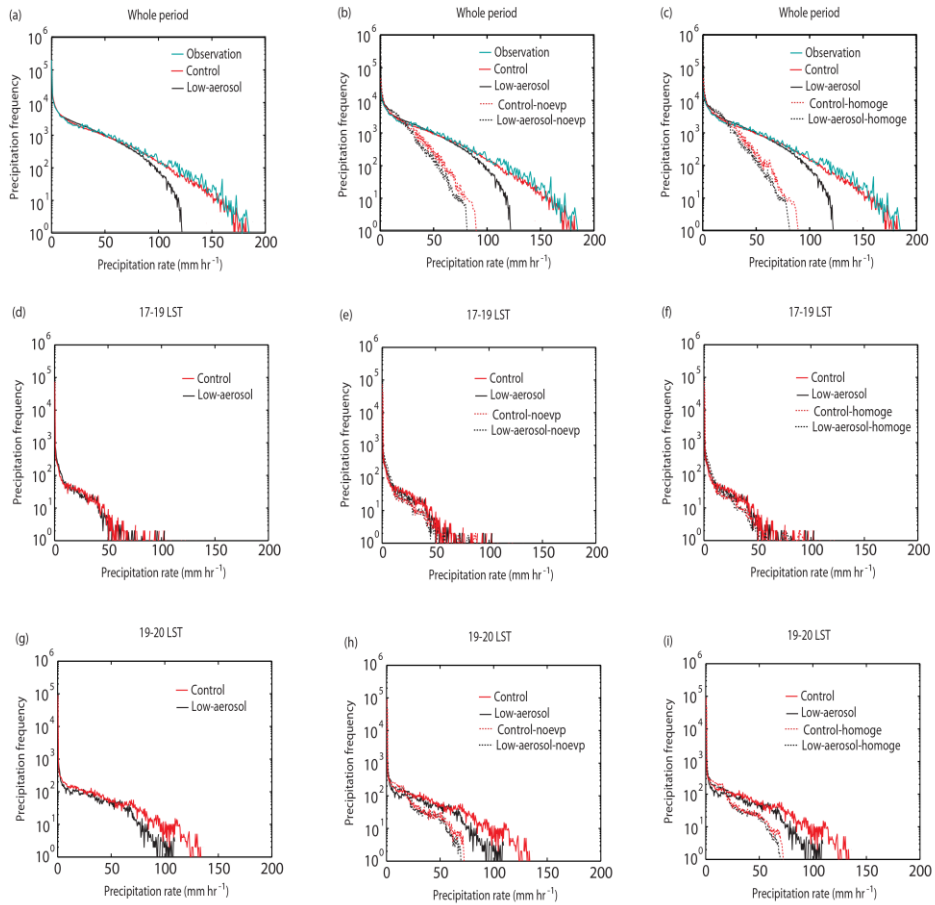
Figure 5



1505

1506

Figure 6



1507

1508

1509

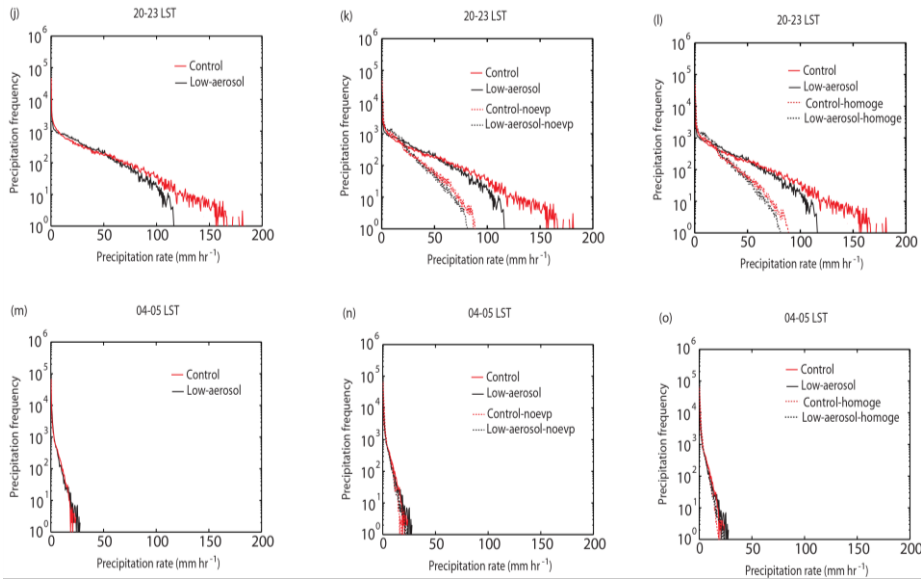
1510

1511

1512

1513

Figure 7



1514

1515

1516

1517

1518

1519

1520

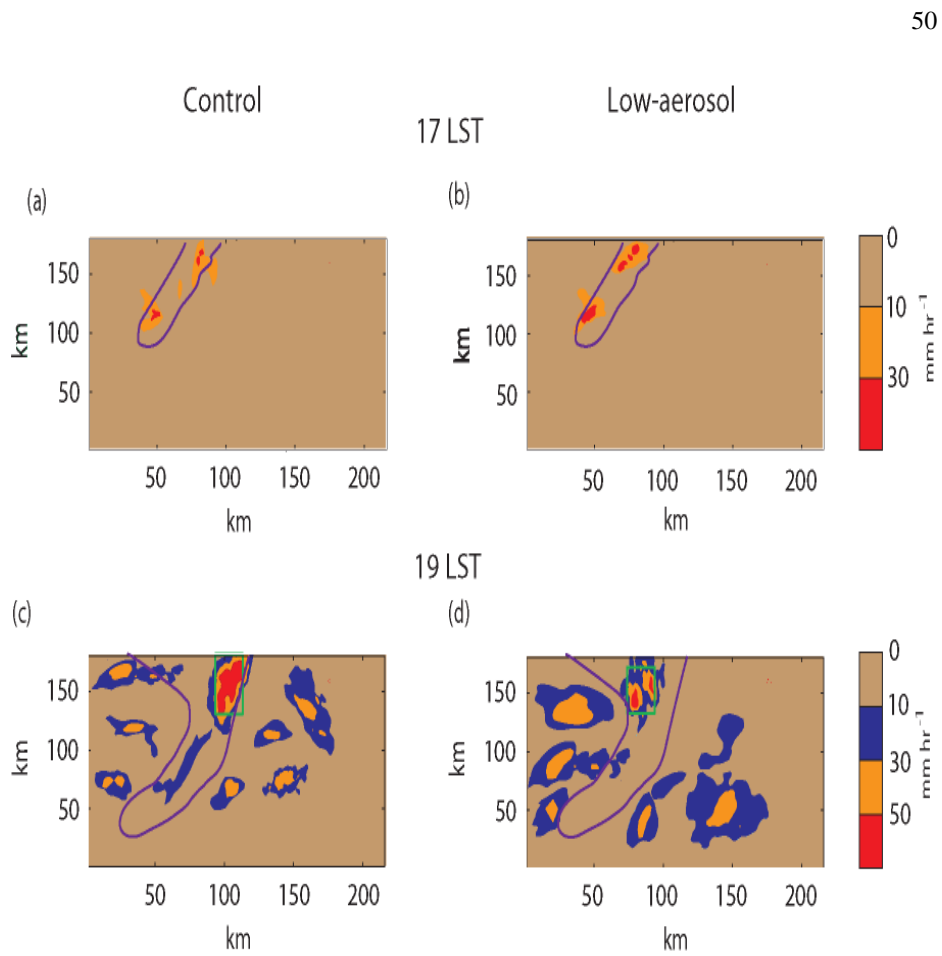
1521

1522

1523

1524

Figure 7



50

1525

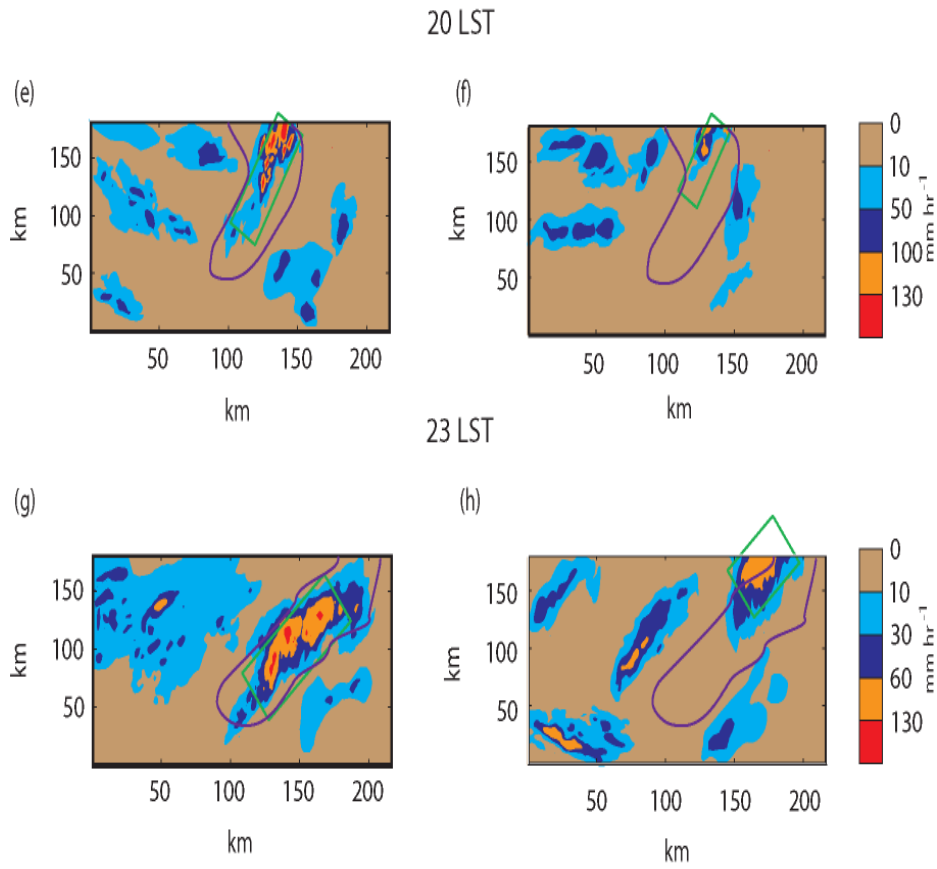
1526

1527

1528

1529

Figure 8

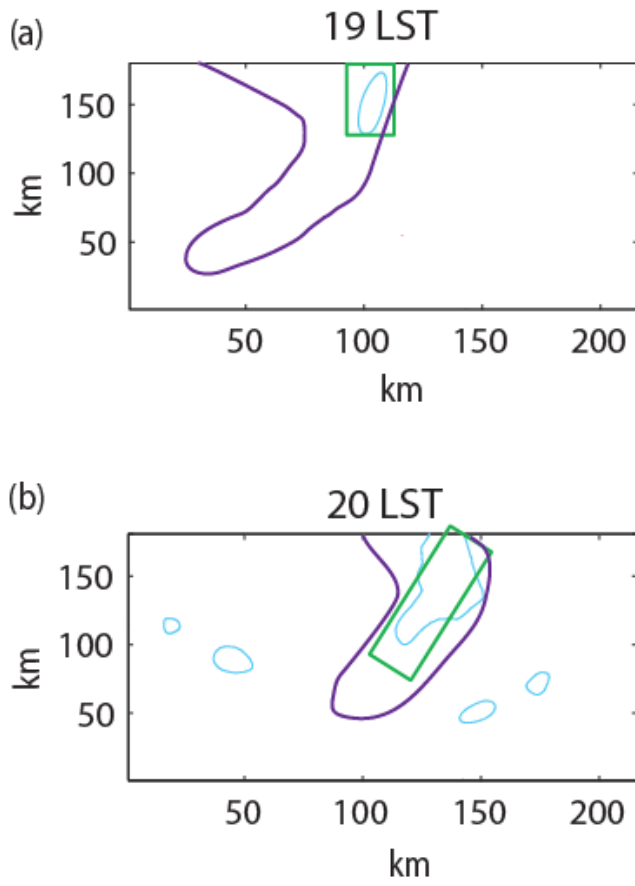


1530

1531

1532

Figure 8



1533

1534

1535

1536

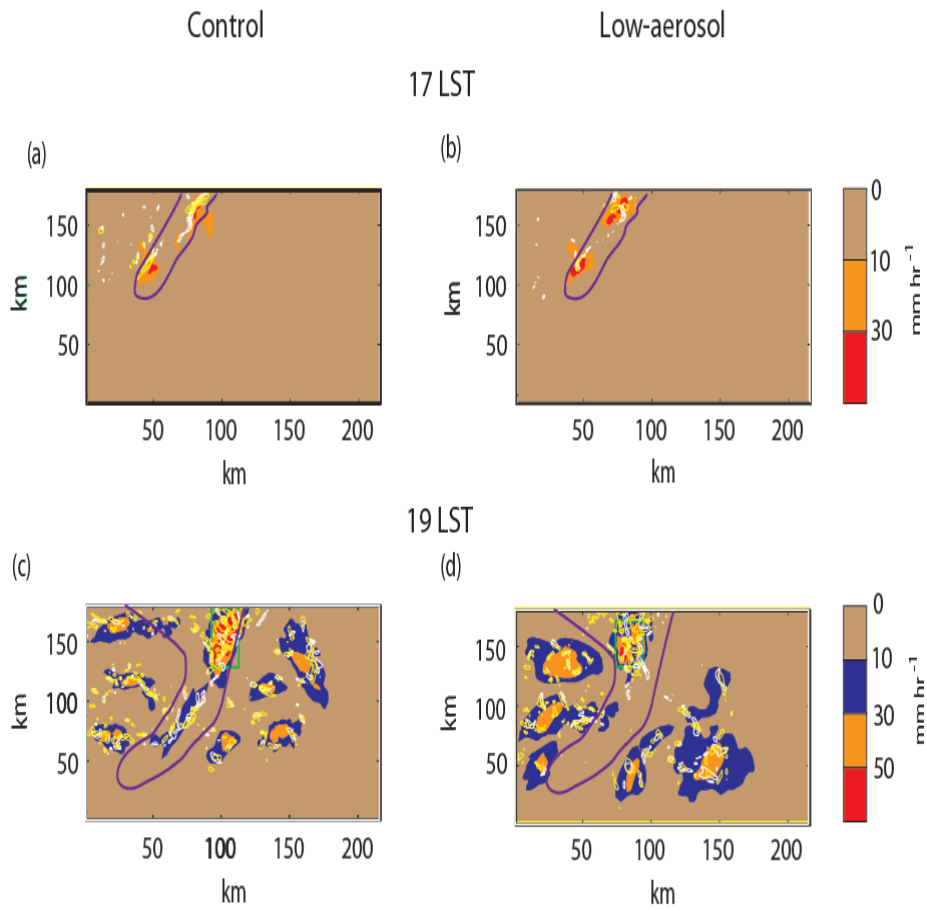
1537

1538

1539

Figure 9

1540



1541

1542

1543

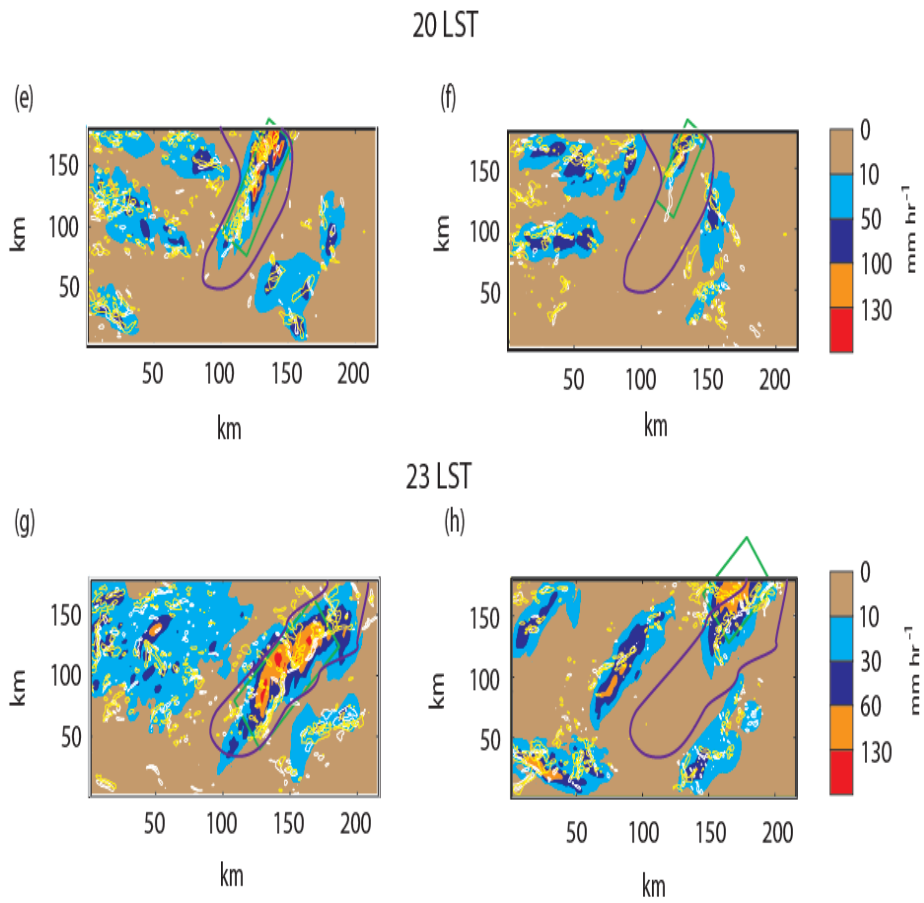
1544

1545

1546

Figure 10

1547



1548

1549

1550

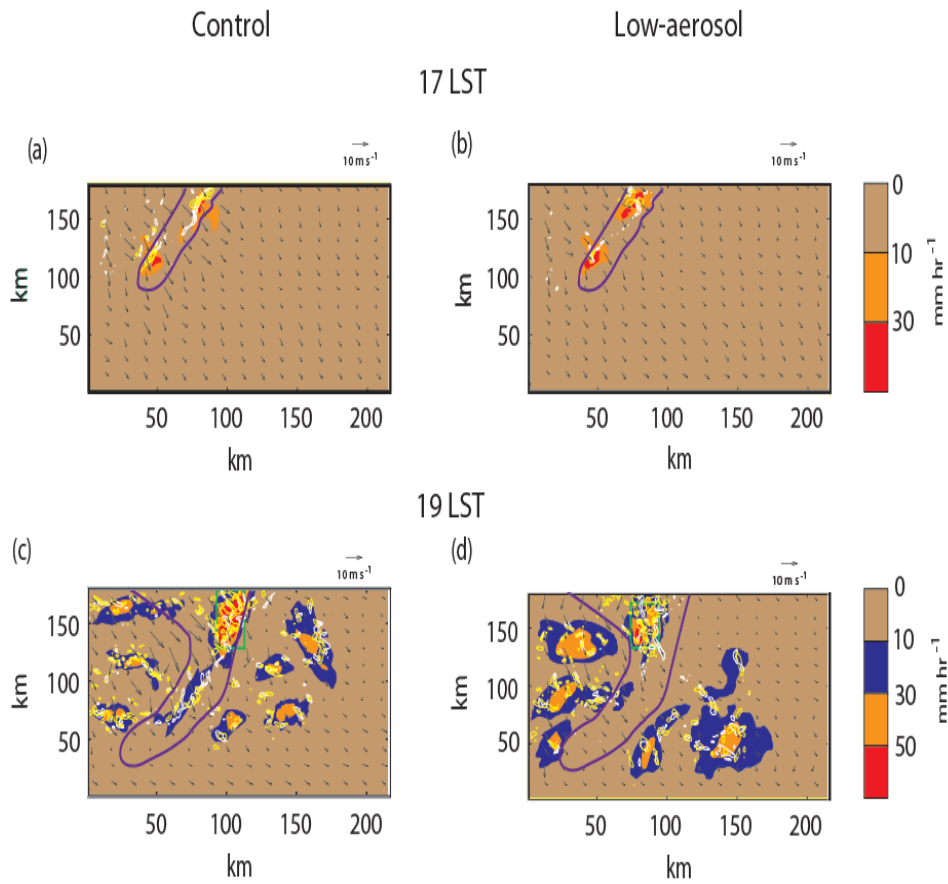
1551

1552

1553

Figure 10

1554



1555

1556

Figure 11

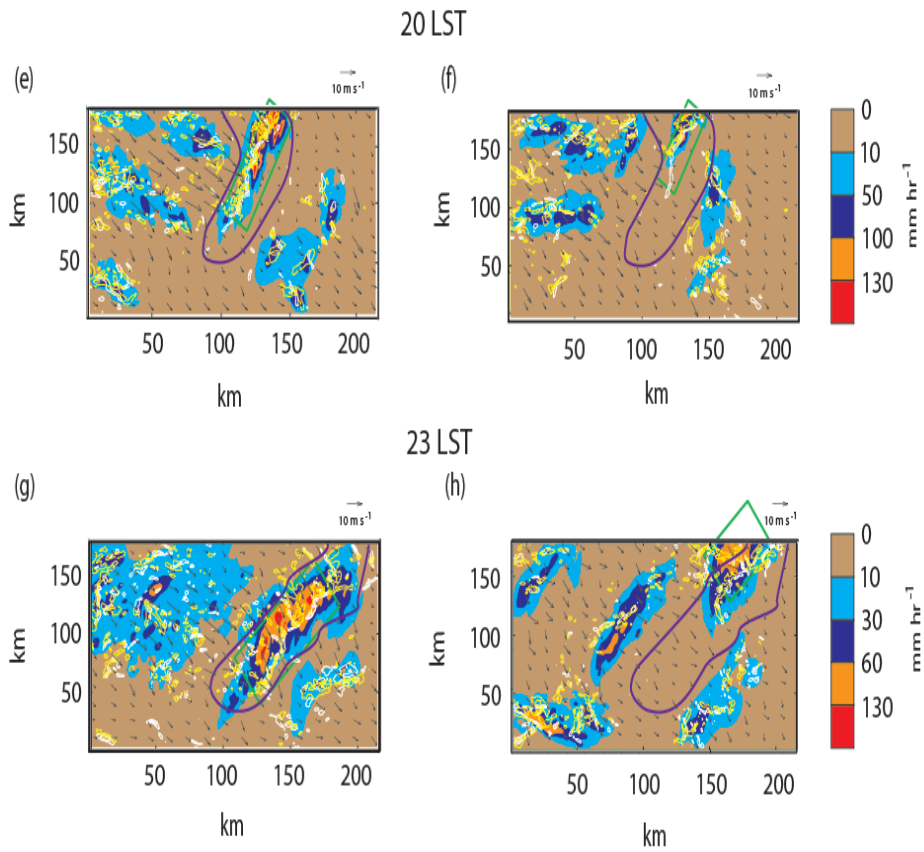
1557

1558

1559

1560

1561



1562

1563

1564

1565

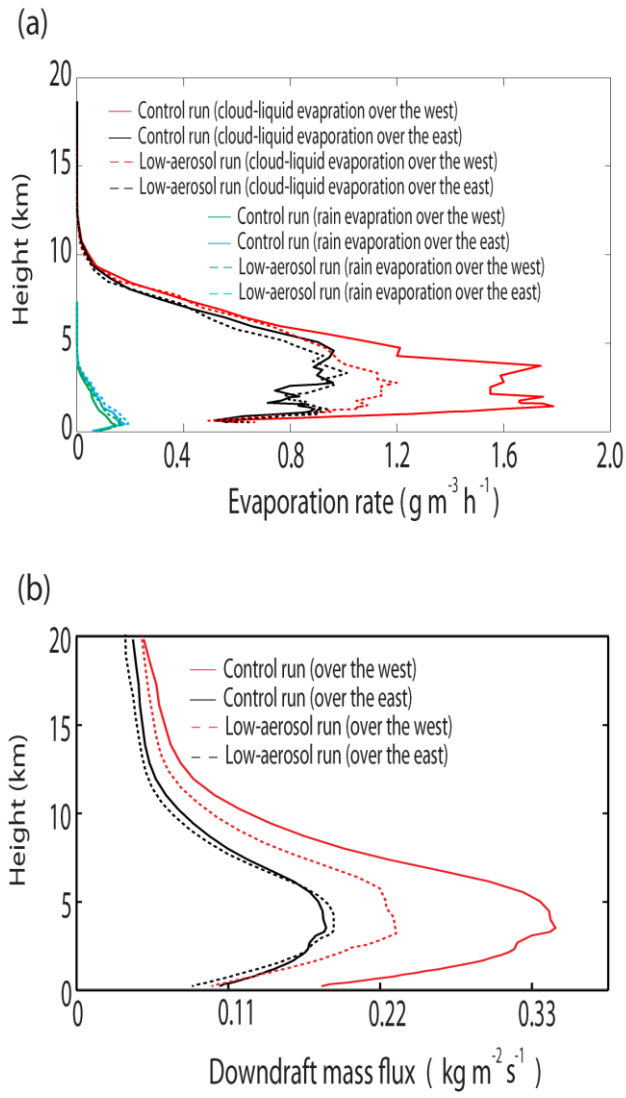
1566

1567

1568

Figure 11

1569

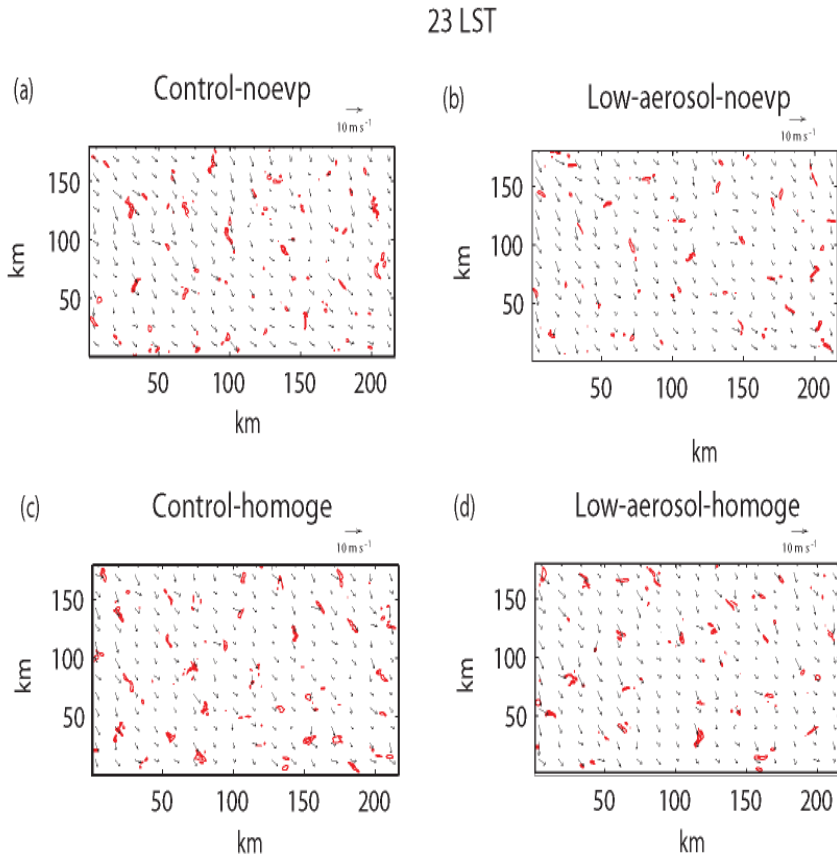


1570

1571

1572

Figure 12



1573

1574

1575

1576

1577

1578

1579

Figure 13